

DESIGN AND FABRICATION OF LOW LOSS AND LOW INDEX
OPTICAL METAMATERIALS

by

Princess MyCia Cox

A dissertation submitted to the faculty of
The University of North Carolina at Charlotte
in partial fulfillment of the requirements
for the degree of Doctor of Philosophy in
Nanoscale Science

Charlotte

2013

Approved by:

Dr. Michael Fiddy

Dr. Patrick Moyer

Dr. Marcus Jones

Dr. Brigid Mullany

©2013
Princess MyCia Cox
ALL RIGHTS RESERVED

ABSTRACT

PRINCESS MYCIA COX. Design and fabrication of low loss and low index optical metamaterials. (Under the direction of DR. MICHAEL FIDDY)

The study of optics has changed over the past 3000 years. We have developed beyond the early lens technologies of quartz and other types of glass materials and new materials are being engineered to enhance the properties of naturally occurring materials through metamaterials. Scattering and propagation of light through subwavelength scale structures can alter the bulk electromagnetic permittivity and permeability of the constituent materials incorporating these nanostructures. Such metamaterials can be modeled and designed to create desired electromagnetic responses such as having a refractive index less than unity. This is the focus of this research using nanoscale low-loss metallic and semiconductor materials. We investigate a new rigorous scattering model for sub-wavelength sized particles that provides a guide that allows bulk materials with reduced refractive index to be made. We show numerical and experimental results supporting this goal.

Using nanoscale low loss semiconductor materials we investigate this scattering model for sub-wavelength sized particles. This approach could lead us to the “Holy Grail” in optical science which is a negative or near zero index material that operates at visible wavelengths.

ACKNOWLEDGEMENTS

I would like to thank my committee chair and advisor Dr. Michael Fiddy for his dedication to this project and for helping me strive to continue this endeavor to the very end. I thank him for his continual spirit of positivity and enthusiasm over this body of work.

I would like to thank my committee members for supporting me through this process and encouraging me to think beyond and go beyond the call of duty as a graduate student.

I would like to thank the professors and graduate students at the University of North Carolina at Charlotte for their insights and support. I would like to thank the Fiddy Research Group for help with numerical simulations, and Dr. Jeffrey Tharp for training and his expertise on HFSS software.

Finally, I would like to thank my mother Dr. R.Cox and my sisters and brothers who have encouraged me and cheered for me every step of the way. This dissertation is dedicated to them and my father Leroy Cox Jr, who has since passed on who taught me to “Strive to do things right, and strive to make things work.”

TABLE OF CONTENTS

LIST OF TABLES	vii
LIST OF FIGURES	viii
CHAPTER I: INTRODUCTION	12
1.1 A Background to Optical Metamaterials	12
1.2 Applications of optical metamaterials	13
1.3 Challenges	14
1.4 Purpose of Study	14
1.5 Statement of the objective	16
1.6 Research questions	17
CHAPTER II: REVIEW OF THE LITERATURE	18
2.1 Metamaterials	18
2.2 Limitations and Assumptions	19
2.3 Examples of Metamaterial	22
2.4 Nanoscale Science and Metamaterials	25
2.5 Synthesis of low-loss nanoparticles	25
2.6 Gold nanoparticles (Au NPs)	26
2.7 Negative Refractive Index Materials (NIMs) (Left Handed Materials)	37
2.8 Refractive Index of Metal Nanoparticles	39
CHAPTER III: METHODOLOGY	42
3.1 Approach	42
3.2 Characterization Techniques	44
3.3 Theoretical Model	45

3.4	Experimental Application of the Theorem	47
3.5	Effective Medium Theories	48
3.6	Numerical construction of Ramm's model	50
3.7	Numerical construction of a low loss metamaterial	53
3.8	Aluminum Doped ZnO (AZO) a low loss material	55
CHAPTER IV: RESULTS		59
4.1	Synthesis of Aluminum Doped Zinc Oxide Nanoparticles	59
4.2	Monitoring Particle Growth	63
4.3	Formation of AZO powders	72
4.4	Constructing the Low Loss Metamaterial	73
4.5	Controlling the assembly of AZO nanoparticles	75
4.6	Measuring the index of AZO nanoparticles	81
CHAPTER V: CONCLUSION		89
5.1	Research objectives revisited	89
5.2	Insights and Interpretations	90
5.3	Future Work	91
5.4	Summary	93
REFERENCES		96
APPENDIX A: MATHEMATICAL CHARACTERS		105

LIST OF TABLES

TABLE 1: Theoretical steps for finding the concentration of particles required for a given target index.	47
TABLE 2: UV-VIS spectrograph measured data from the Al-Doped ZnO during synthesis using the ethanol wash method.	62
TABLE 3: UV-VIS spectrograph measured data from the Al-Doped ZnO during synthesis using the water wash method.	65
TABLE 4: Dynamic Light Scattering measured data of Al-Doped ZnO during synthesis in relationship to particle growth using the ethanol wash method.	66
TABLE 5: Dynamic Light Scattering measured data of Al-Doped ZnO during synthesis in relationship to particle growth using the water wash method.	67
TABLE 6: Emission spectrograph measured data from the Al-Doped ZnO during synthesis using the ethanol only wash method.	70
TABLE 7: Emission spectrograph measured data from the Al-Doped ZnO during synthesis using the water wash method.	71
TABLE 8: Size of AZO nanoparticles using ethanol wash synthetic technique after adhesion of octadecylamine.	77
TABLE 9: UV-VIS spectrographs of AZO nanoparticles using the ethanol wash synthetic technique before and after ligand adhesion of octadecylamine.	79
TABLE 10: Mathematical Characters	105

LIST OF FIGURES

FIGURE 1: Metamaterial Tree of Knowledge (Zheludev, 2010).	19
FIGURE 2: Gold SRR electron micrograph (Klein, 2006).	22
FIGURE 3: SRR compared with LC circuit(Linden, 2011).	22
FIGURE 4: Gold Metal Fishnet Structure Simulation (Zhang, 2005).	23
FIGURE 5: Fishnet Structure (Zhang, 2005).	24
FIGURE 6: Permittivity of 15 nm gold nanoparticles (Stoller, 2006).	26
FIGURE 7: Wurzite structure model of ZnO with tetrahedral coordination of Zn-O (Wang, 2004).	35
FIGURE 8: Electronic band structure of ZnO showing it as a direct band gap material (Ozgar, 2005).	35
FIGURE 9: Illustration for (a) positive and (b) negative refraction for a light-ray incident on a material with $ n_2 > n_1 $. In (a) $0 < n_1 < n_2$ and in (b) $0 < n_1 < n_2 $ and $n_2 < 0$ (Ward, 2005).	38
FIGURE 10: Material parameter space characterized by electric permittivity and magnetic permeability (Liu , 2010).	39
FIGURE 11: Index change of gold nanoparticles dependent on volume fraction of gold nanoparticles relative to the host medium (Kubo, 2007).	40
FIGURE 12: Experimental measurements of the dielectric constants for silver particles (Pei,2010)	40
FIGURE 13: CuCl nanoparticles array (Yannopapas, 2008).	41
FIGURE 14: Matlab numerical prediction of the target index as a function of the log of the number of particles per liter for gold nanoparticles values from Johnson and Christy, 1972.	50

FIGURE 15: Matlab numerical prediction of the target index as a function of the log of the number of particles per liter for gold nanoparticles between 10^{17} to 10^{20} , values for the target index from Johnson and Christy, 1972.	51
FIGURE 16: Matlab numerical prediction of the target index as a function of the log of the number of particles per liter for gold nanoparticles values from Stoller, 2006.	52
FIGURE 17: Matlab numerical prediction of the target index as a function of the log of the number of particles per liter for gold nanoparticles between 10^{17} to 10^{20} , index values from Stoller, 2006.	52
FIGURE 18: HFSS power reflection data of Gold nanoparticles with 50 nm radius.	54
FIGURE 19: HFSS data for center-to-center spacing of gold nanoparticles as a function of resonance response.	54
FIGURE 20: HFSS model of AZO with an increasing conductivity vs. particle separation.	57
FIGURE 21: HFSS model of 20 nm radius AZO nanoparticles.	58
FIGURE 22: UV-Vis spectrograph of Al-Doped ZnO with variation in the mole percentage of aluminum. The growth of the nanoparticles is seen with variation with time using the ethanol wash method.	63
FIGURE 23: UV-VIS spectrograph of Al-Doped ZnO with variation in the mole percentage of aluminum. The growth of the nanoparticles is seen with variation of time using the water wash method.	65
FIGURE 24: Dynamic Light Scattering histogram of 1% Al-Doped ZnO during synthesis in relationship to particle growth using the ethanol wash method.	67
FIGURE 25: Dynamic Light Scattering histogram of 3% Al-Doped ZnO during synthesis in relationship to particle growth using the ethanol wash method.	68
FIGURE 26: Dynamic Light Scattering histogram of 6% Al-Doped ZnO	68

during synthesis in relationship to particle growth using the ethanol wash method.

- FIGURE 27: Emission spectrographs of Al-Doped ZnO with variation in the mole percentage of aluminum. The growth of the nanoparticles is seen with variation of time using the ethanol wash method. 70
- FIGURE 28: Emission spectrographs of Al-Doped ZnO with variation in the mole percentage of aluminum. The growth of the nanoparticles is seen with variation of time using the water wash method. 72
- FIGURE 29: Illustration of the refraction of light at the interface of two mediums. 74
- FIGURE 30: Illustration of measuring the refractive index using a 1.5 micron laser source and detector. 74
- FIGURE 31: Dynamic Light Scattering histograms of AZO nanoparticles size using ethanol wash synthetic technique after adhesion of octadecylamine. (A) 1% Al-doped (B) 3% Al-doped (C) 6% Al-doped. 77
- FIGURE 32: UV-VIS spectrographs of AZO nanoparticles using ethanol wash method before and after octadecylamine ligand adhesion. 78
- FIGURE 33: Infrared spectrograph of 1% AZO nanoparticles using ethanol wash method after adhesion of octadecylamine. 80
- FIGURE 34: Infrared spectrograph of 1% AZO nanoparticles using ethanol wash method before ligand adhesion. 80
- FIGURE 35: Photograph of AZO nanoparticles evaporated on to the surface of the IR detector. 81
- FIGURE 36: Scanning electron micrograph of 1% AZO particles. 82
- FIGURE 37: Scanning electron micrograph of 3% AZO particles. 82
- FIGURE 38: Scanning electron micrograph of 6% AZO particles. 82
- FIGURE 39: COMSOL model representation of 100 nm AZO nanoparticles. It shows a COMSOL realization of a quadrupole resonance amongst 4 nanoparticles of AZO. 83

FIGURE 40: COMSOL numerical predictions of the real part of the index for 100 nm AZO nanoparticles with interparticle spacing between 0.5-100 nm.	84
FIGURE 41: Index of 1% AZO thin film using UV-NIR Ellipsometer.	86
FIGURE 42: COMSOL numerical predictions of the imaginary part of the index for AZO nanoparticles with interparticle spacing between 0.5-100 nm.	86
FIGURE 43: Index of refraction of silicon wafer using UV-NIR Ellipsometer.	87
FIGURE 44: Permittivity of 1% AZO using UV-NIR Ellipsometer.	87

CHAPTER I: INTRODUCTION

1.1 A Background to Optical Metamaterials

Metamaterials are artificially engineered structures that are designed to change the propagation of electromagnetic waves. People have been altering electromagnetic waves for centuries based upon material composition; this is commonly seen in lens and mirror technologies. A significant difference in metamaterials is that they are specifically designed to exhibit unusual electromagnetic properties and are endeavoring to exhibit controlled responses. To understand this concept of unusual electromagnetic properties we need to define those properties as they relate to permittivity and permeability. Permittivity is the measure of the response of the medium to the electric field and permeability is the measure of the material's response to the magnetic field. For metamaterials this response can be changed depending on the orientation of the subwavelength-scaled features used to build a metamaterial, namely "meta atoms". The meta atoms are engineered elements that have designed electromagnetic resonances and then are assembled into periodic or random arrays to give composite materials. These meta atoms have a resonance response since near resonance, dispersion relations dictate that a significant change in the effective permittivity and /or permeability of the medium can be found.

In 1927 the Nobel prize was awarded for the significance of defining these dispersion relations, known as the Kramers-Kronig relations. Any variation of the real

parts of the permittivity and/or permeability (and hence refractive index which is just the square root of the product of these two parameters) with frequency is accompanied by variation in the imaginary part.¹ It thus connects the absorption or gain of a resonance or material's electromagnetic response to the refractive index. This is a fundamental consequence of the fact that the polarizability of any material is a causal function.

Based on an appreciation of how to engineer structures exhibiting such resonances, researchers have conceptualized and realized some unusual electromagnetic properties such as magnetism at optical frequencies, negative refractive index, large positive refractive index, zero reflection through impedance matching, perfect absorption, giant circular dichroism and enhanced nonlinear optical properties.²

1.2 Applications of optical metamaterials

The potential applications of optical metamaterial are still being revealed since the potential to make materials not found in nature is almost limitless. For example, using metamaterial surfaces that exhibit optical magnetic responses or which behave as perfect absorbers have been recently proposed. For the latter, light is neither reflected nor transmitted over certain frequency bands for a broad range of angles, and this could have significant contributions for light harvesting and hence to the solar cell industry, (Soukoulis, 2011) .

The metamaterial research community is actively exploring metamaterials whose dielectric constants are engineered or even dynamically tuned, to provide, for example bulk negative index materials. In these both the permittivity and permeability are designed to be negative. Researchers have discovered numerous applications for negative index materials such as superscatterers, high resolution imaging systems, optical

concentrators and also cloaking technologies based on transformation optics. When a structure is covered or coated by a low index material and then illuminated by an incident wave, one can realize a reduction in the scattering cross section of that structure. The coating reduces the reflections over a wide band of angles and frequencies. The scattered field can be reduced and applications in optics, infrared, THz and radar technology are very exciting. ³

The application of high resolution imaging of subwavelength features using optical metamaterials is developing quickly and holds enormous promise for biological and medical research since one could then avoid invasive techniques for discovering cellular processes.

1.3 Challenges

Even though these applications are intriguing and the implications are vast, there are some challenging questions that must be addressed in their design and fabrication. These resonant meta atoms needs to be smaller than a wavelength and ordered in an array with variation in geometric orientation to exhibit these electromagnetic properties for these optical metamaterials. Lithographic techniques have been used to design and fabricate these materials but these processes are expensive. The other challenge is fabricating these structures on a large scale in 3D. The next question is how can we overcome these challenges?

1.4 Purpose of Study

Nanoscale science, nanotechnology and nanoscale materials emerged and became well established research themes in the latter half of the 20th century. Advances have been rapid, driven by new cutting edge synthesizing techniques for creating

nanostructures such as carbon nanotubes, metal oxides, and metallic and bimetallic, and various nanoarchetypes.

A key reason the scientific community has devoted so much effort to the creation of nanomaterials is the enormous potential for these materials within applied sciences and commercial development. For example, the work done by Louis E. Brus who discovered colloidal semiconductors known as “quantum dots”, has transformed research in transistors, light emission diodes (LEDs), solar cells and diode lasers^{4, 5}.

Now researchers are combining nanoscale materials with metamaterials science. Scientists are using nanoscale materials to form new types of metamaterials. Some of these metamaterials contain conducting elements and can be modeled as inductance (L) and capacitance (C) circuits to predict the bulk properties of metamaterials that use nanoscale materials.⁶ It has been shown that the influence of metal nanoparticles or semiconductor nanoparticles can have a significant effect on the electromagnetic response of such metamaterials.

However, our interest relies on the most fundamental nanoscale materials which are metal colloids, semiconductors, and colloidal gold. By using nanoscale materials as a component of a nanoscale composite material we plan to control the permittivity and permeability of the material and thus alter its bulk index of refraction.

We are exploiting the quadrupole resonance of clusters of four or more nanoparticles, and so while there is some flexibility in their location, we need them sufficiently close to be able to induce this resonance. Also this approach can be realized in a bulk manufacturing context; subwavelength particles do not need to be equidistant. We propose to apply this method to make a bulk solid material (over whatever optical

frequency interval is of interest) having an index close to zero. In a solid material with this refractive index, form birefringence will then allow index values $0 < n < 1$ to be realized.

A rigorous theoretical model has been developed by Dr. Alexander Ramm⁷, to describe scattering from a medium of sub-wavelength scaled particles ($ka \ll 1$). A recipe has been developed which allows one to specify the desired refractive index of a bulk metamaterial made of these particles. The theory requires that we can characterize and fabricate particles in terms of their surface boundary impedances or refractive indices.

Low index materials (i.e. $n < 1$) are very important for a large number of applications. This new rigorous theoretical approach allows any index to be specified in principle, low or high but it remains a theory and ours will be one of the first attempts to reduce its predictions to practice. The theory applies to acoustic materials as well.

1.5 Statement of the objective

To use nanoscale metallic materials following a new rigorous scattering model that provides a recipe that allows bulk materials with a prescribed index to be made. Our hypothesis explores resonant meta-atoms and does not require at this point LC circuit representations and are attractive for realizing these properties in a bulk manufacturing context; we note that subwavelength particles do not need to be equidistant.

We propose to incorporate aspects of this method and make a bulk solid material (over whatever frequency interval is of interest) having an index close to zero; form-birefringence will then allow index values $0 < n < 1$ to be realized.

1.6 Research questions

Can a material with an index of less than unity be realized by increasing a material scattering properties to drive down the index, and by altering particle-particle separation?

Is this material predicted using Dr. Ramm's theoretical model or by well known mixing formula?

Can High Frequency Structure Simulations (HFSS), COMSOL Multiphysics, and Matlab provide supporting or predictive evidence for experimental findings?

CHAPTER II: REVIEW OF THE LITERATURE

2.1 Metamaterials

Metamaterials are artificial materials that are designed to have new fundamental characteristics differing from the conventional materials. In Greek the word “meta” means after or beyond. In naturally occurring materials their electromagnetic responses are characterized by the quantum energy levels of the atoms or molecules. Metamaterials offer us the potential to control these interactions with electromagnetic waves. The electromagnetic properties of a metamaterial are typically attributed to the resonant characteristic of the sub wavelength scaled meta-atoms comprising the materials; at optical frequencies plasmonic effects can be exploited.⁸

Metamaterials differ from structured periodic materials comprised of approximately wavelength-scaled repeating units which rely on multiple Bragg scattering. Metamaterials may be dependent on single or multiple scattering phenomena but the meta-atoms spacing is much smaller than the operational wavelength. It is the collection of these components that may or may not be periodic, that contribute to the bulk magnetic and electric responses. In (Figure 1) the tree shows the possible fruits that metamaterials can produce. Invisibility through transformation optics, imaging with unlimited resolution through negative index materials (NIMs) are just a few of the possible fruits yet to be ripened and picked.

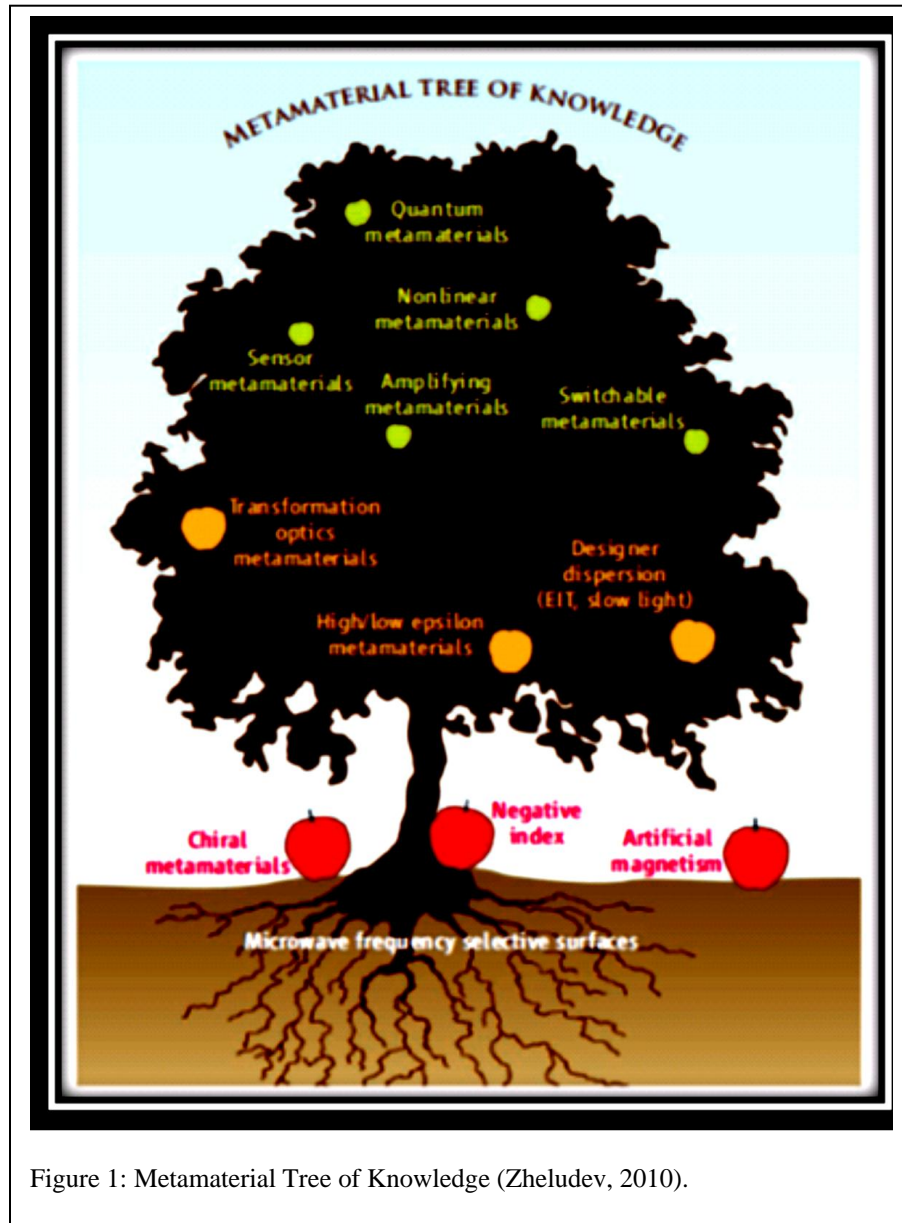


Figure 1: Metamaterial Tree of Knowledge (Zheludev, 2010).

2.2 Limitations and Assumptions

The challenges for metamaterials are (1) the high losses that can occur when resonant phenomena are exploited, (2) designing the permittivity and permeability of the bulk material based on the properties of individual elements, and (3) fabrication challenges, especially for optical metamaterials. In classical electromagnetism, material

properties can be described by the Lorentz-Drude model (Equations 1, 2). The subscripts e and m represent the electric and magnetic responses for this frequency dependent model. Gamma is the damping constant that accounts for the loss in the material. This model serves as a guide to describe how to engineer the electromagnetic properties, specifically the permittivity and permeability of the metamaterial.

$$\varepsilon_{r(\omega)} = 1 - \frac{\omega_{p,e}^2}{\omega^2 - \omega_{0,e}^2 + i\gamma_e\omega}$$

Equation 1

$$\mu_{r(\omega)} = 1 - \frac{\omega_{p,m}^2}{\omega^2 - \omega_{0,m}^2 + i\gamma_m\omega}$$

Equation 2

The primary challenge is reducing the bulk material loss, specifically for many metallic metamaterials which are increasingly strong absorbers at lower frequencies. Looking at this model it can be surmised that for noble metals if we take the free electron approximation into account, the permittivities of these metals can be negative below the plasma frequency. However, causing the magnetic response (permeability) to be negative is much more difficult. The magnetic response is more pronounced at lower frequencies and weak at optical frequencies. This is due to the weaker circulating currents that can be generated at higher frequencies.⁹

For this reason, many experiments with metamaterials are being conducted for example within the X-band (microwave regions) since metamaterial models are easier to validate. For example, metamaterials with a negative refractive index are of great interest since Pendry demonstrated that negative index materials (NIMs) can be used to make a perfect lens with resolution not limited by diffraction.¹⁰ Pendry was one of the first to propose practical applications for the use of metamaterials. In his work he used a thin silver slab to approximate a negative index material and focus all Fourier components of

a 2D image. A negative index metamaterial can be realized in the microwave region but Pendry and others see the value in having this capability for the optical region of the electromagnetic spectrum.

Pendry found that a sufficiently low loss negative index slab would amplify the evanescent waves within the slab and thus contribute to a super resolved image.

Because the meta atoms in metamaterial have to be considerably smaller than the wavelength, current methods of fabricating optical metamaterials are electron-beam lithography (EBL), focused-ion beam (FIB) milling, nanoimprint lithography (NIL) and possibly interference lithography (IL) and direct laser writing.¹¹

The challenge is fabricating features sizes smaller than 100 nm and periodicities or spacing's of this size or smaller. Another concern is when writing large areas, the production time and cost increases considerably.

Electron-beam lithography is still the choice method for fabrication for very high resolution features over approximately a $100\mu\text{m} \times 100\mu\text{m}$ area. However, when designing three dimensional metamaterial structures; alternative methods such as two-photon photo polymerization techniques (TPP) may be the future. TPP offer sub-diffraction resolution down to 100 nm due to a nonlinear multi-photon process.¹²

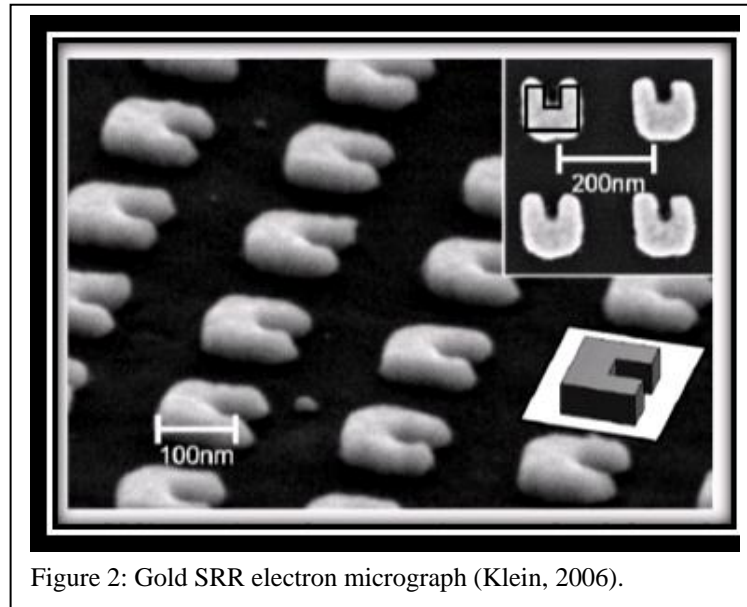


Figure 2: Gold SRR electron micrograph (Klein, 2006).

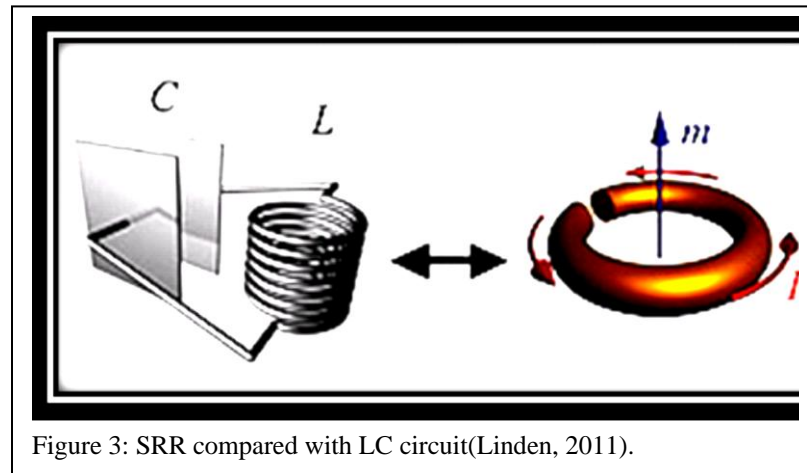


Figure 3: SRR compared with LC circuit(Linden, 2011).

2.3 Examples of Metamaterial

2.3.1 The Split Ring Resonator

One of the most interesting meta-atoms used in a metamaterial in the past decade is the Split-Ring Resonator (SRR) proposed by Pendry in 1999. The SRR is designed to

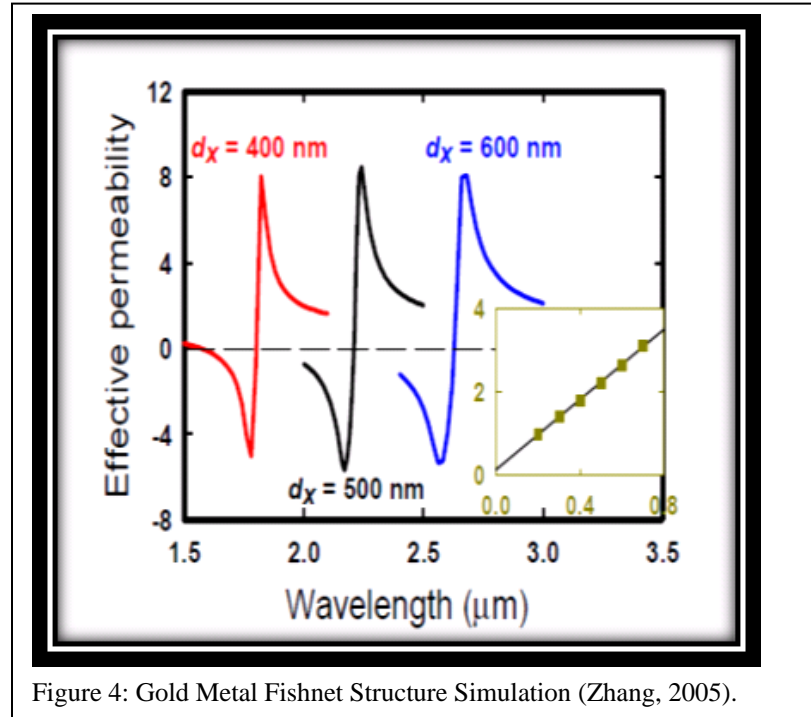


Figure 4: Gold Metal Fishnet Structure Simulation (Zhang, 2005).

control the magnetic responses indicative of the electromagnetic wave.¹³ The SRR can be viewed as a typical LC circuit shown in Figure 2 and 3.¹⁴ The SRR acts as a planar resonant circuit in which the oscillating electric current is induced by the light. The result is a magnetic dipole which is normal to the plane of the ring. When the SRRs are densely packed the magnetic dipoles couple together as well as induce a macroscopic magnetization. The electric current can be induced in two ways; by a time-dependent magnetic flux or by an electric-field component of the light parallel to the slit of the ring.¹⁵ Creating an artificial magnetic response at terahertz and optical frequencies is a challenge. The geometrical scaling of the particle resonant frequency breaks down at higher frequencies for SRRs.^{16, 17} The kinetic energy of the conduction band electrons become increasingly important at these frequencies and thus manipulating the magnetic response becomes difficult. For a single SRR the magnetic response starts to break downs

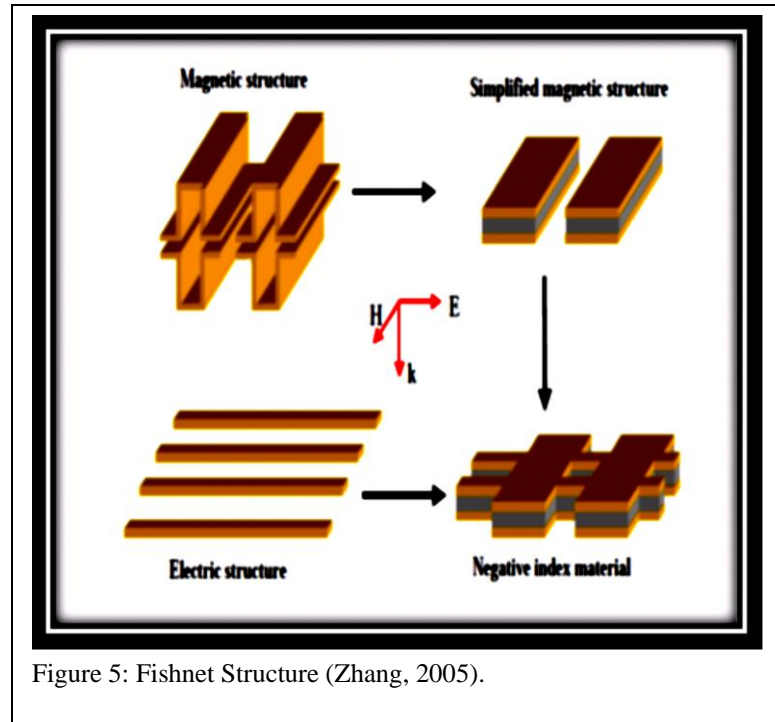


Figure 5: Fishnet Structure (Zhang, 2005).

for frequencies higher than 200 THz, and the metal deviates from an ideal conductor.

¹¹One of the ways in overcoming this barrier is to alter the shape of the SRRs, by changing the distance between the rings' ends and minimizing the cross-sectional area of the ring.¹⁸

2.3.2 Fishnet Metamaterials

The SRR proposed by Pendry morphed into a fishnet type structure introduced by Zhang in 2005.¹⁹ This structure allowed for the possibility of controlling the magnetic component at optical or near infrared frequencies. In Figure 4 the magnetic response is altered by layering nanorods with a dielectric in a grid like pattern or fishnet to induce the necessary magnetic response. The metal strips generate a magnetic resonance that is originated by anti-parallel currents in the metal strips. To obtain $\epsilon < 0$ and $\mu < 0$ with overlapping spectral regions the fishnet metamaterial was proposed. Figure 5 shows how the effective permeability goes negative ($\mu < 0$).

2.4 Nanoscale Science and Metamaterials

The type of material used is important in metamaterial science. The optical properties such as diffraction, polarization, transmission, and reflectance for example rely to a degree on the atomic element being used. The metamaterial depends more so on the equivalent circuit and its resonant frequencies that the meta-atom represents. Just as for antenna technology strongly relying at microwave frequencies, the metamaterials the meta-atoms used can be as large as millimeter to micron in size scale.

Creating metamaterials at the nanoscale would allow the creation of materials that operate at optical wavelength scales. This would increase the likelihood of finding new metamaterials for optical frequencies.

We will briefly discuss some of the past and future synthetic procedures for fabricating nanoscale materials specifically nanoparticles/nanospheres for creating a new generation of metamaterials.

2.5 Synthesis of low-loss nanoparticles

Low-loss nanoparticles are materials that are dielectrics that marginally inhibit the propagation of electromagnetic waves. Determining what materials exhibit this behavior we can look at two classifications of the material, the permittivity and conductivity. The following mathematical statement must hold true for this material noted in equation 3.

$$\frac{\sigma}{(\omega\epsilon')} \ll 1$$

Equation 3

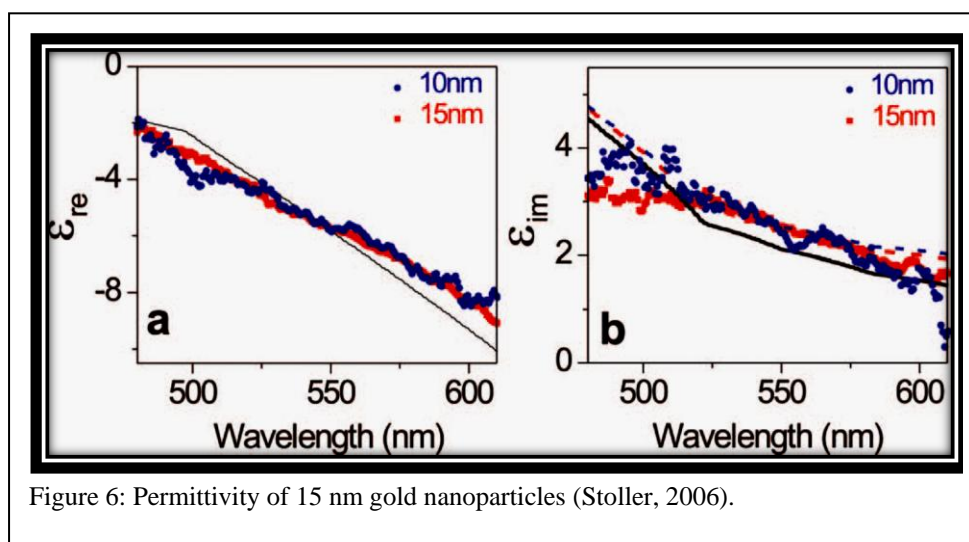
For nanoparticles the loss term or (imaginary part of the permittivity) will be dependent on the frequency. So, the material is not only a dielectric but conveys a dispersive property.

We found three materials of interest but experimentally chose to follow one material for a computational comparative study. The materials were Gold, Silver and Aluminum doped Zinc Oxide (AZO).

2.6 Gold nanoparticles (Au NPs)

In the literature we found that for 15 gold nanoparticles of 15 nm in radius the index was $0.84+1.2i$ at 515 nm according to Stoller et al.²⁰ (Figure 6) For a thin film of gold with a thickness of 343 Å (angstroms) the optical constants at 589 nm was $0.29+3.01i$ according to Johnson and Christy et al.²¹ Even though, the loss term was high we conducted several experiments to determine whether gold would meet our need to have a material index less than unity.

Gold is the 79th element in the periodic table. It is a soft metal and has many interesting properties that have been studied for centuries. In history colloidal gold was used in making stained glass windows. In 1857, Michael Faraday made colloidal gold by the reduction of gold chlorate with phosphorous in carbon sulfide. He studied the optical properties of thin gold films during this time. Recently renewed interest of gold materials



has sparked a wave of synthetic the techniques for producing colloidal gold and nanoparticles of gold. The methods performed by Gunter Schmid and Michael Brust, et al.²²

There are several techniques for fabricating gold colloids; however there are physical fundamentals that are important in fabrication. There are several factors that affect colloidal growth; reducing agents, ligands, particle concentrations, temperature, and dispersion solvents.

Reducing agents donate electrons to gold allowing the species to reach a zero valence state. This zero valence state is necessary for cluster formation and growth. The ligands stabilize the gold clusters and prevent aggregation of the species by chemically adsorbing on the surface of the clusters. The concentrations of these reactants play a large role in the formation of your particle. For instance if you increase the concentration of your metal salt for synthesis you will increase the salt ions resulting in Van der Waals force causing aggregation or precipitation of your species.²³

Monolayer Protected Cluster consists of a gold metal that has been surrounded by a ligand to stabilize its structure. In 1994 Brust used ligands with sulfur functional groups to form MPCs of sizes less than 3 nanometers in scale. The ligands self-assemble onto the surface of the gold clusters, sulfur atoms has an affinity.

2.6.1.1 Synthetic Methods

There are numerous synthetic methodologies for fabricating nanoscale materials. The following section describes a few common methods and their details. However, many scientists rely upon a culmination of methods to achieve their desired results.

2.6.1.2 Citrate Reduction

In 1951 John Turkevich and others published a paper called “Nucleation and Growth Process in the Synthesis of Colloidal gold”. In this paper was a description of a method to create colloids of 20 nm size. This method was further enhanced by G. Frens who extended the synthesis of these water soluble particles from 16-147 nanometers.²⁴ This method allows for the synthesis of Au NPs by the reduction of gold salts by disodium citrate to allow for the assembling of stabilizing ligands. In detail, Gold hydrochlorate in aqueous solution is boiled to 100 °C; preheated sodium tris-citrate is added to the solution with continual stirring. The solution is cooled to room temperature and exposed to UV radiation.²⁵ Using this method the size and shape of the particle can be influenced by the concentrations and type of reductant used as studied by various researchers.

In a study by Kimling, UV radiation was used to assist particle growth. The upper limits of trisodium citrate concentrations of 0.05-1.6 mM were studied. They found that by increasing the concentration the stability of the smaller particles were increased, and that lower concentrations produce aggregation. When speaking in term of stability of the particular species of interest it should be noted that in the absence of a stabilizing ligand the species formed will aggregate or even disperse to its original metal structure.

The Turkevich method is also used for synthesis of Nanowires by citrate reduction of AuCl₄ as discussed in the article by Pei. Nanowires of a two-dimensional network are synthesized by modification of the citrate reduction. Sodium tetrachloroaurate is stirred in temperature controlled oil bath to 80°C. Trisodium citrate is rapidly added to the solution at controlled molar concentrations of 0.1-2.7. They found

that lower concentration of sodium citrate formed more stable 2-Dimensional networks of gold nanowires.²⁶

Another similar technique involving the method established by Turkevich is to form gold nanoparticles by bromoaurate reduction using amino acids. Amino acids were dissolved in potassium hydroxide and to this mixture added drop wise KAuBr_4 at room temperature.²⁷

The gold Nanoparticles were water soluble and it was discovered that a mixture of the two amino acids glycyl-L-tyrosine and L-tyrosine showed a distribution of particles sizes proportional to the ratio of the L-amino acids. The particles were roughly spherical in their shape. From this article we can see a role of gold nanoparticles using biofunctionalized ligands.

2.6.1.3 Brust Method

In 1994 Mathias Brust and others wrote an article entitled “Synthesis of Thiol-derivatized Gold nanoparticles in a Two-phase Liquid-Liquid System”. In this article a synthesis of gold nanoparticles of organic derivatized particles are formed. The process involved mixing aqueous gold hydrochlorate with tetraoctylammonium bromide which transfers the aqueous gold into the organic phase. The gold is then reduced by sodium borohydride in the presence of dodecanethiol which assembles on the surface of the gold thus forming Self Assembling Monolayers.²⁸ These particles were predominantly cuboctahedral and icosahedral structures ranging in size from 1-3 nanometers. The particles that were formed were stable over several weeks. What was remarkable was Au formed in large amounts. This new technique has allowed for the synthesis of stable gold

nanoparticles of sizes less than 5 nanometers which differs from the Turkevich method of synthesis.

There are several examples of synthesis of gold nanoparticles of various sizes and shapes using this two-phase method. $\text{Au}_{38}[\text{PhCH}_2\text{CH}_2\text{S}]_{24}$ can be synthesized by varying concentrations of reductant and the thiol-functionalized ligands. One approach uses a 3:1 ratio of thiol to gold and a 10:1 ratio of reducing agent to gold.²⁹ Au_{38} was synthesized by using the Brust procedure and a single-phase procedure. Key features of the Brust procedure used is that after the reductant was added the solution was stirred at 0°C for 24 hours. The isolation of the product had many steps. First the aqueous reductant separated from the organic phase Monolayer Protected Clusters (MPCs) and excess was washed out with nanopure water. The solution was evaporated and acetonitrile was added for extraction of the product overnight. The acetonitrile soluble material is collected and evaporated and re-dissolved in ethanol and filtered to remove impurities. The Au_{38} was purified again by re-dissolving in methylene chloride and precipitating the crystals by 80/20 ethanol-water mixture and filtering on a fine glass frit. The acetonitrile insoluble material from their analysis was Au_{140} . In another synthesis of Au_{38} in this same research group, the article by Jimenez discusses the synthesis of Au_{38} by using hexanethiol ligands.

This Brust synthesis involved a comparative study of the nucleation and passivation by lower temperature and excess ligands.³⁰ In both approaches Au_{38} was produced but isolation of a pure substance was an issue. When isolating Brust-type synthesis of nanoparticles of less than 1.6 nanometers in core diameter. Low yields of product and isolation of a pure product are key issues in production. The Brust method of gold nanoparticles synthesis does not centrally gravitate towards production of Au_{38}

clusters. Depending on the conditions of the reaction medium larger particles can also be generated.

2.6.1.4 Sonolysis

Sonolysis is a method for the formation of gold nanoparticles using ultrasound irradiation of a gold hydrochlorate solution containing glucose. The radicals produced from this method act as reducing agents and orient the gold molecules in such a way to produce nanoribbons and or nanobelts.³¹

2.6.1.5 Electrolysis

Gold nanoparticles can also be formed of various shape and size by electrolysis. In this approach nanowires are produced by the electrochemical reduction of gold hydrochlorate in the presence of a capping agent (ligand).^{32,33} One synthesis procedure described involves a two-electrode cell consisting of a rotating platinum rod as the cathode and a platinum sheet as the anode. The electrolytic solution consisted of potassium nitrate, gold hydrochlorate and poly(N-vinylpyrrolidone) (PVP). The temperature was approximately 22°C and the current was 100 mA. This technique employed by Huang et al produced a large yield of material with small amount of byproducts.

2.6.1.6 Seed-Growth

This technique uses small nanoparticles to initiate the growth of larger particles that that they are distributed evenly in size. Although the Brust method is widely used for the synthesis of smaller nanoparticles size, the same method for producing larger nanoparticles results in a wide distribution of sizes.³⁴ In this method Au ions (precursor) are reduced during the reaction and nucleate at the surface of the seeds. By carefully

controlling the ratio of seed to metal salt (growth solution) and the reduction speed, Au nanoparticles ranging from 5–40 nm are produced.³⁵

2.6.1.7 Laser Ablation

The gold nanoparticles synthesis method formed by Henglein discovered that gold in solution could be ablated by a laser to produce gold colloids.³⁶ An example of this form of synthesis is the formation of gold nanoparticles by immersing a gold plate in solution of sodium dodecyl sulfate and ablating the target metal with the laser.³⁷

Depending on the intensity of the laser nanoparticles of various sizes from 1-5 nm can be produced.

2.6.1.8 Sol-Gel

The gold salt is transferred to the organic phase by tetraoctylammonium bromide then gravimetrically incorporated into the sol-gel. The sample is allowed to rest and then is irradiated with UV radiation that reduces the gold salt and allows the growth of gold nanowires.³⁸

2.6.1.9 Template Synthesis

In this process mesoporous silica films are prepared on glass plates. The films are then coated with the gold nanoparticles. The nanoparticles formed are ordered to this structure. The silica films are then removed with acid leaving gold nanoparticles behind.³⁹

Of the various methods of nanoparticles and nanowires synthesis this is promising in that it produces uniform materials.

2.6.2 Silver Nanoparticles

Silver is a material that has a large permittivity in respect to gold but at several wavelengths the loss term is marginal. The types of synthetic methods are the same for gold nanoparticles fabrication.

2.6.3 Zinc Oxide Nanoparticles

2.6.3.1 Zinc Oxide Properties and Applications

Zinc Oxide (ZnO) is an inorganic material that is stunning industries across the globe for its utility as a II-VI compound semiconductor. It has been used in sun protections, pigment for paints, photovoltaic solar cells, porcelain enamels, heat resistant glass, and as a protective coating for spacecraft. Some of the other technical applications have been in catalytic studies and sensor technology and biomedical sciences, optoelectronics and transducers to name a few.^{40, 41}

There has been a current influx of interest in ZnO nanostructures such as epitaxial layers, quantum dots, quantum wells, nanorods with the hope to obtain;

A material for UV optoelectronics (light-emitting or laser diodes), a material for electronic circuits that is transparent in the visible, transparent conducting oxide (TCO) when doped with Aluminum (Al), Gallium(Ga), or Indium(In) as cheaper substitutes to Indium Tin Oxide (ITO).⁴²

Zinc oxide has been studied since the early 1900's and its chemistry, physical nature, and optoelectronic qualities have been well known and characterized. The lattice-dimensions of zinc oxide found in 1935 using X-Ray powder photographs were: $a_0 = 3.2426_5 \pm 0.0001$, $c_0 = 5.1948 \pm 0.0003$, axial ratio $c_0/a_0 = 1.6020_0 \pm 0.0001$, all at 18°C.⁴³

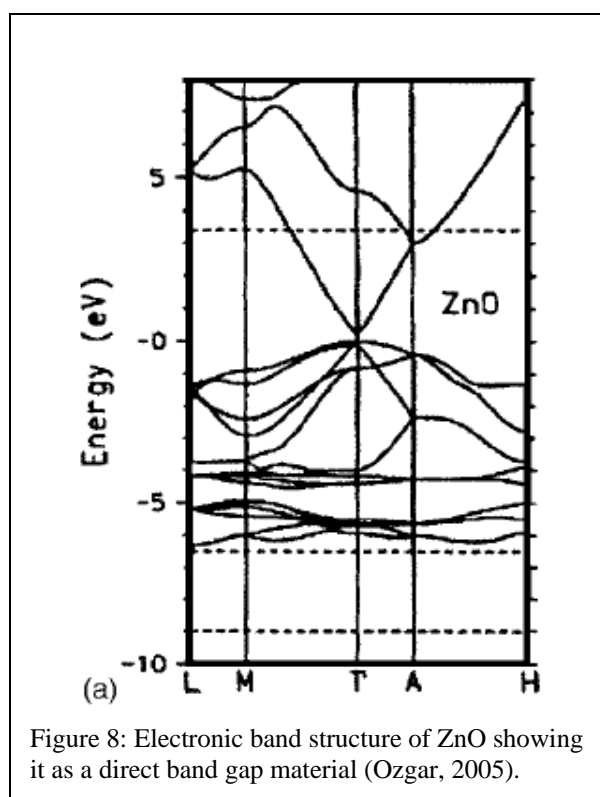
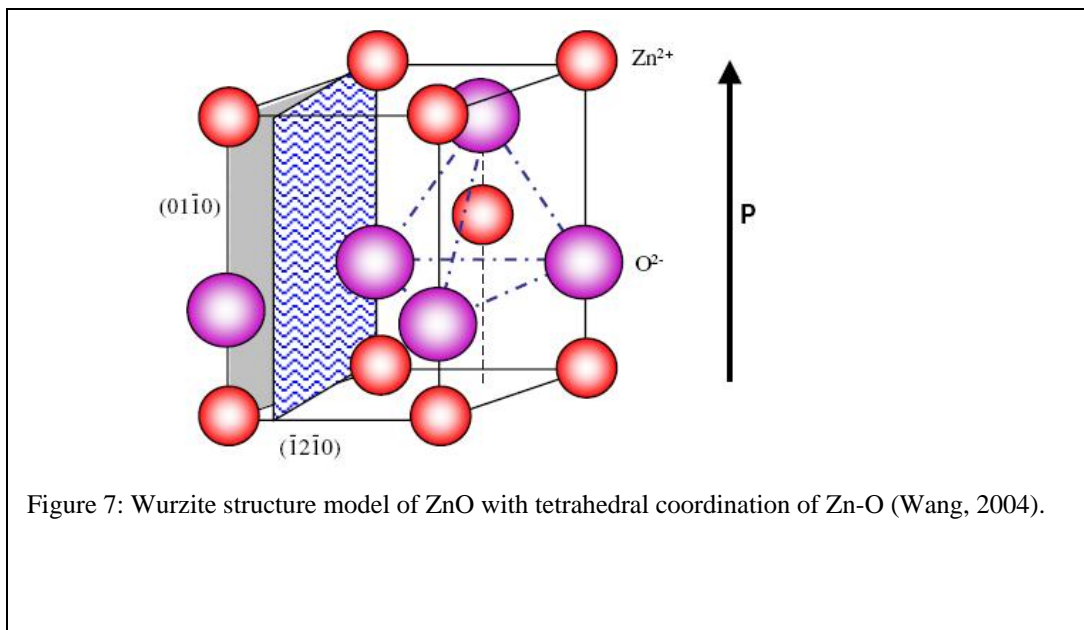
2.6.3.1.1 Crystal Structure of ZnO

ZnO is a II-VI compound semiconductor with three main crystal structures; wurzite, zinc blend and rocksalt. ZnO has tetrahedral sp^3 covalent bonding with ionic bonding character as well. The common Wurtzite zinc oxide has a hexagonal structure with alternating planes of tetrahedral coordinated O^{2-} and Zn^{2+} ions that are stacked. This non-central symmetric structure gives ZnO its piezoelectric and pyroelectric character and it also lack center inversion. ZnO exhibits crystallographic polarity this indicates the direction of the bonds and for zinc blend and rocksalt it is close-packed (111) planes and for wurzite it has basal planes (0001), (Ozgur, 2005) The wurzite crystal structure of ZnO can occur in nature and the mineral Zincite.

2.6.3.1.2 Electronic Band Structure

Zinc Oxide has a wide band gap that is around 3.37 eV at 300K and 3.44 at low temperatures.⁴⁴ The free exciton binding energy of ZnO is 60 meV.⁴⁵⁻⁴⁷ Zinc oxide is a direct band gap materia (Figure 7) which means that the electron mobility in the conduction band is high and that the bottom of the conduction band occurs where effective momentum (k) is equal to zero. This can change if the ZnO is a nanoparticle in particular a nanowire/nanorod. In these cases the band gap can transition from directed to indirect.⁴⁸

The Hall carrier concentration of bulk ZnO is $6 \times 10^{16} \text{ cm}^{-3}$ at 300K and the mobility is $205 \text{ cm}^2 \text{ V}^{-1} \text{ s}^{-1}$.⁴⁹



2.6.3.1.3 Electrical Conductivity

ZnO has n-type conductivity and has strong luminescence. The origin or mechanism is still being researched, however it is thought to be attributed to the oxygen vacancies and zinc interstitials.^{50, 51}

2.6.3.2 Synthesis of ZnO Nanoparticles

The production of bulk zinc oxide powders or films is well known and their methods of production are straightforward. There are several methods/techniques for the growth of bulk crystals of ZnO. There is hydrothermal growth⁵²⁻⁵⁵, vapor-phase transport^{56, 57} and pressurized melt growth.^{58, 59} Films of ZnO can be done by chemical vapor deposition (MOCVD)⁵⁹⁻⁶², molecular-beam epitaxy⁶³⁻⁶⁵, laser ablation⁶⁶ or sputtering.⁶⁷

The synthesis of ZnO nanoparticles/nanomaterials is more arduous. However, some of the bulk crystal growth methods have been carefully used by scientists in their formation. We will take a look at these methods in more detail and process some of the benefits and challenges presented to material scientists.

2.6.3.2.1 The Sol-Gel Process Synthesis of Colloidal ZnO nanoparticles

This process became well known in the 1990s by Spanhel and Anderson who utilized biological techniques and grafted them on to nanofabrication. The method involves three steps; (1) preparation of organometallic precursor, (2) preparation of ZnO colloids, (3) concentration of ZnO colloids into syrups or aerogels.⁶⁸ In their synthesis it involved zinc acetate dihydrate and lithium hydroxide as the organometallic precursors. The result of this type of synthesis resulted in particles less than 10 nm in radius.

2.7 Negative Refractive Index Materials (NIMs) (Left Handed Materials)

Another important aspect of metamaterials is the design of negative index materials. As we aspire to drive the index in these materials from the positive to less than one, we can consider pushing forward to negative index values.

In 1967, Veselago⁶⁹ wrote in a Russian journal an expression for the refractive index in terms of relative permittivity (ϵ) and permeability (μ), that would allow each term to be negative (Equation 3). However, in 1957 the same conclusions that Veselago reached were reached earlier by Sivukhin.⁷⁰ Veselago's paper is considered to be one of the forerunners for the beginning of the subject matter of NIMs and metamaterials. This 1967 paper was re-discovered in 2000 by Smith⁷¹ and has launched the world of optics in a tailspin according to some scholars. This has been compounded by John Pendry from the Blakett Laboratory at Imperial College in London, England in regards to using these materials to make a perfect lens.

$$n = \pm\sqrt{\epsilon_r\mu_r}$$

Equation 4

Veselago discussed in his paper the possible outcomes of ϵ and μ being simultaneously negative in relation to the fundamental axioms of Maxwell's equations (Equation 4).

$$\mathbf{k} \times \mathbf{H} = -\frac{\omega}{c} \epsilon \mathbf{E} \quad \text{and} \quad \mathbf{k} \times \mathbf{E} = \frac{\omega}{c} \mu \mathbf{H}$$

Equation 5

For both material constants to be negative, Maxwell's equations imply that the materials will have a negative group velocity. If the wave vector and the pointing vector are in opposite directions, a backward-wave material would result. This will lead to an inverse Snell's law, Doppler Effect and Cerenkov Effect. To illustrate how a negative index material might behave Figure 9 shows Fermat's Principle of Least Time.⁷² The figure represents the path that light will travel in the least amount of time through the NIMs.

Some of the basic components for NIMs are as follows: the dielectric constants ϵ and μ characterize the macroscopic response of a homogeneous medium to an applied electric and magnetic field. If the meta-atoms comprising the metamaterial are smaller than the wavelength of radiation, and the bulk material's electromagnetic response exhibits unusual properties, then it can be said to be a metamaterial.

The dielectric permittivity and permeability are dispersive and have complex components associated with the frequency. This means that $\epsilon(\omega)$ and $\mu(\omega)$ are related by

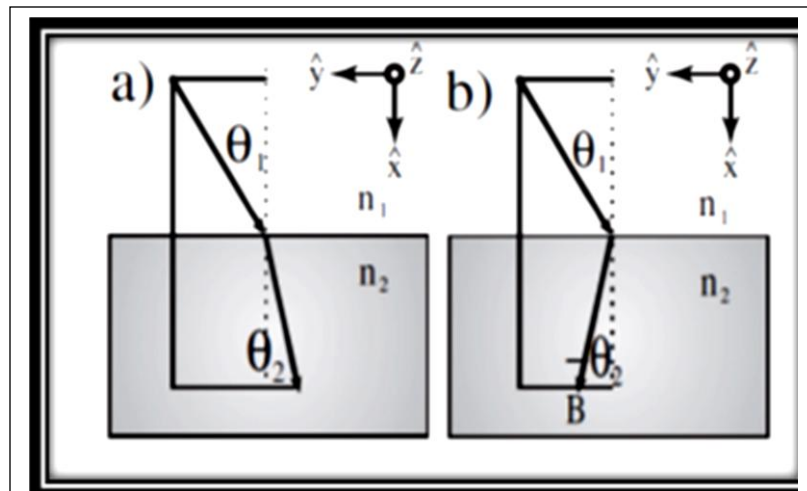
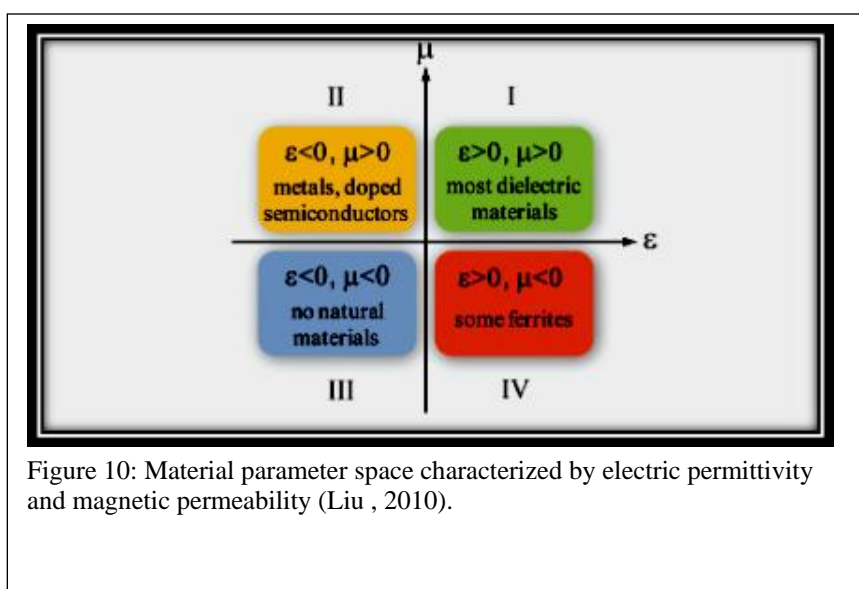


Figure 9: Illustration for (a) positive and (b) negative refraction for a light-ray incident on a material with $|n_2| > |n_1|$. In (a) $0 < n_1 < n_2$ and in (b) $0 < n_1 < |n_2|$ and $n_2 < 0$ (Ward, 2005).

the Kramers–Kronig relationship. The imaginary parts of these dielectric constants relate directly with the absorption of radiation of the material.⁷³

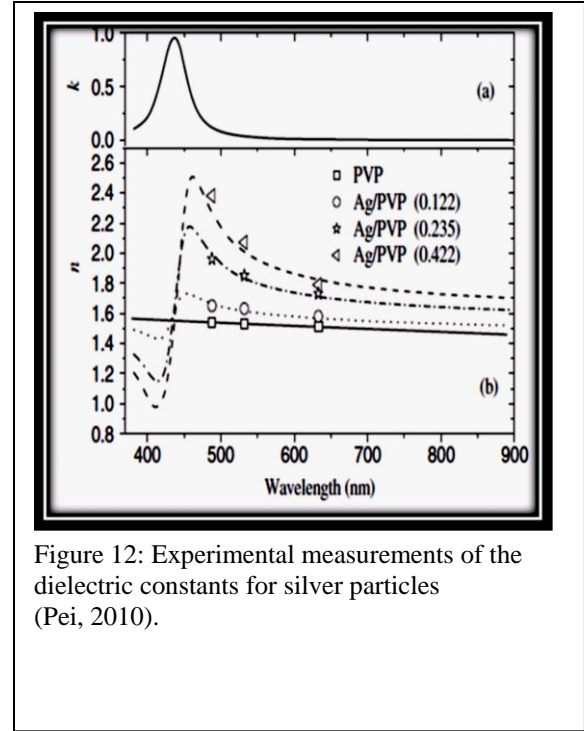
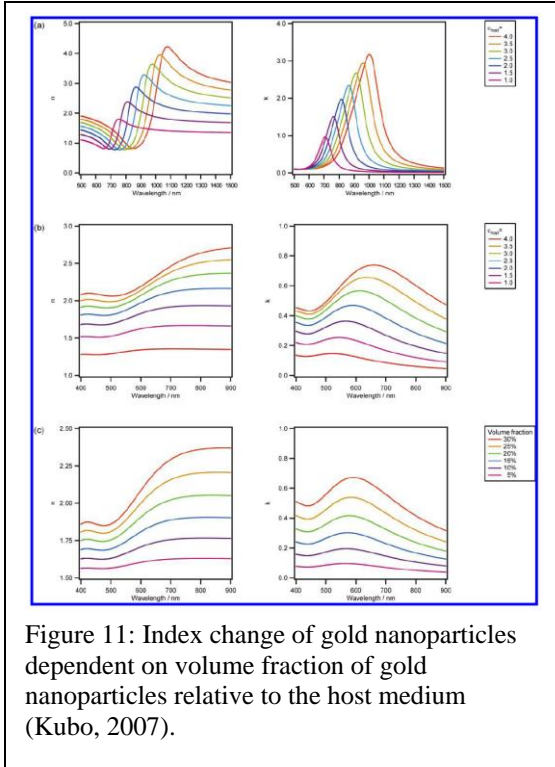
2.8 Refractive Index of Metal Nanoparticles

In 1972, Johnson and Christy did a great deal of research in determining experimentally the refractive index of thin metal films.²¹ Current researchers have used



their data to collaborate their experimental data and findings with nanoparticles and metamaterials.

Researchers have found that the indexes of nanoparticles, specifically gold and silver, are determined by their surrounding media. In 2007, Kubo and his collaborators conducted work involving modeling and experimentally deducing the effects on the dielectric constants as a result of altering the host medium for silica/gold nanoparticles 40 nm in diameter see Figure 11.⁷⁴ This study showed that the macroscopic characters of the



electromagnetic field in the material are dependent on the concentration or the packing density of the meta-units in the material. This is consistent with the conclusions in the Ramm model. Pei and his co-workers fabricated a mixture of silver nanoparticles with polyvinyl pyrrolidone to create a film that was cast onto a glass slide.⁷⁵ In Figure 12 we see that $dn/d\omega$ has a steep slope when the volume fraction of this composite mixture is increased. This steep slope infers that a negative group velocity (Equations 6 and 7) is possible for this material, which is indicative of a negative index material.

$$n = \frac{ck}{\omega} \text{ then } \frac{d\omega}{dk} = \frac{c}{\omega} \left[\frac{n}{\omega} \frac{dn}{d\omega} \right]^{-1}$$

Equation 6

$$v_g = \frac{c}{n + \omega \frac{dn}{d\omega}} = \frac{c}{n_g}$$

Equation 7

For a negative index, not only does the slope need to be negative but the magnitude of the slope must be greater than n/ω . In Figure 13 the same distinct sharp slope is seen for a 3D array of closed packed CuCl nanoparticles with 28 nm diameter.⁷⁶ So, it can be confirmed from the literature, as expected, that there is an effect of concentration and packing sequence of meta-atoms on the macroscopic character of the electromagnetic response of the material.

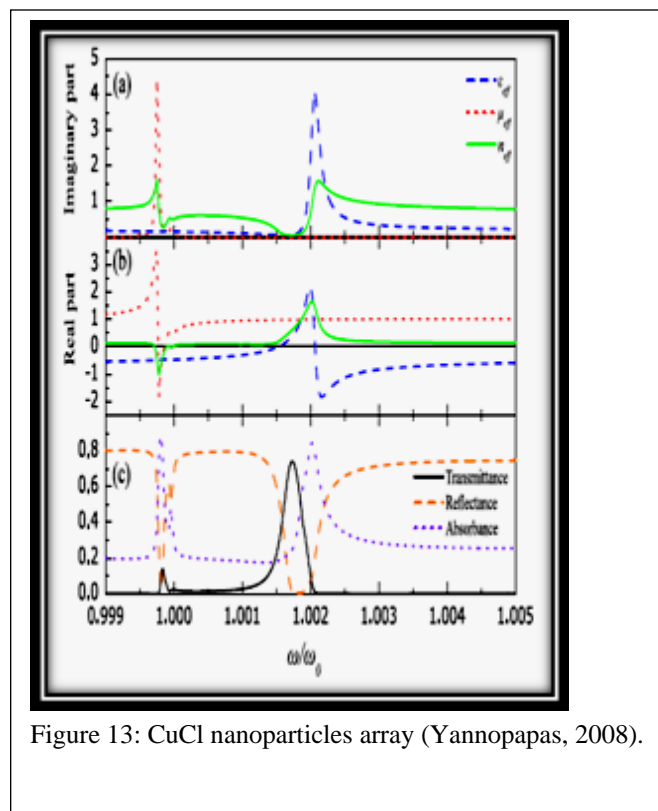


Figure 13: CuCl nanoparticles array (Yannopapas, 2008).

CHAPTER III: METHODOLOGY

3.1 Approach

Metal nanoparticles in a host medium influence bulk permittivity and permeability. One of the ways this is determined is by measuring the index of refraction. In 1972 Johnson and Christy did extensive research involving thin metal films of gold and determined the index of refraction experimentally.²¹ Their data compilations are still being used today, but our knowledge of the index of refraction of nanoparticles themselves is still limited. While there are several experimental techniques used to determine the index of refraction of nanoparticles however, there is less data on individual particles. This lack of experimental data is a challenge for our research interest. One of the methods we have used is to rely on computation simulations to exercise the technical data needed.

The fundamental principles of this research rely on the “recipe” created by the work done by Alexander Ramm from 1980 to the present. The scattering dynamics of small bodies can be described by surface boundary impedance that can be determined from the measured scattering amplitude. The recipe gives the concentration of these particles that is necessary to create a desired refractive index response. As the particle size goes to zero the recipe and prescribed index value becomes more accurate from a theoretical perspective.⁷⁷

We know from Mie and Raleigh scattering theories that it is possible to mathematically deduce the scattering response of particles.^{78, 79} We intend to use data generated from instruments that measure light scattering to determine the scattering amplitude of the particles described by Ramm, thus the surface boundary impedance will be determined. The surface boundary impedance is a part of the model to input a desired refractive index.

3.1.1 Research Objectives

There are five main experimental research objectives that must be achieved for the goal of making a low index optical material to be realized.

1. Synthesis of metal nanoparticles by well-established methods in the literature; then determine the surface boundary impedance of these particles from their scattering amplitudes.
2. Prepare different concentrations of these particles in a transparent host and compare measured index values with theory.
3. Determine the effect of coatings (e.g. ligands) on measured surface boundary impedance values.
4. Develop bulk materials with increasing particle concentrations to approach an index close to zero (useful for many applications by exploiting form-birefringence).
5. Determine the changes in the bulk refractive index as a function of the particle surface impedances and as the particles grow in solution during synthesis thus altering their concentration.

3.2 Characterization Techniques

3.2.1 Structural Characterization

3.2.1.1 Scanning Electron Microscopy (SEM)

In order to characterize the nature of nanopowders, or nanofilms the scanning electron microscope can be utilized. The instrument can measure within 10 nm of a particle if it is high resolution. The SEM works by using a high energy beam of electrons that is focused on the surface of the samples. The beam scans across the surface and a detector collects the data.

3.2.1.2 Dynamic Light Scattering

Dynamic light scattering has the ability to characterize the size and molecular weight of small particles. It is more easily used for spherical particles, but biologist use it to measure the molecular weight of proteins and other biological assays. The instrument measures the change in the light as it scatters off of the particle, and using several classical electromagnetic theories it can determine the size of the particle.

3.2.2 Optical Characterization

3.2.2.1 Ultra-Violet Spectroscopy (UV-VIS)

The UV-VIS measures the amount of light that is absorbed by a species. For nanomaterials a strong peak in the UV range is a strong indicator of colloidal particles. It can also be used to determine the concentration of your sample material utilizing Beer's-Lambert laws.

3.2.2.2 Fluorescence

The fluorimeter measures the amount of light that is emitted when the material is excited by light. The material absorbs the light and the photons of that material are

excited. A detector then measures the intensity of the electronic emissions from the material.

3.2.2.3 Transmission Spectroscopy

This is one of the easiest techniques for measure optical properties of samples. A white light source is passed through a monochromator and the change in intensities of the light is collected by a detector. This can be used to measure the transmittance and reflectance of samples in the Near Infrared and Infrared .

3.3 Theoretical Model

The following recipe (method) describes how to calculate the number of nanoparticles (i.e. small inhomogeneities) per unit volume to achieve a given bulk index. The origins of the model are taken from the publications of Dr. A. Ramm. The embedding of the inhomogeneities in a bound space results in a system of equations describing a desired scattering potential (i.e. bulk refractive index).

Step 1

$$\{n^2(x)n_0^2(x)\} \Rightarrow p(x) = k^2(n_0^2 - n^2)$$

Step 2

$$\text{Given } p(x) = p_1 + ip_2, \text{ find } \{h(x), N(x)\}$$

$$\text{Here } h(x) = h_1(x) + ih_2(x), N(x) \geq 0, h_2(x) \leq 0$$

$$\text{We have } p(x) = 4\pi N(x)h(x)$$

$$\text{Thus } h_1(x) = \frac{p_1(x)}{4\pi N(x)}, h_2(x) = \frac{p_2(x)}{4\pi N(x)}$$

There are many solutions, because $N(x) \geq 0$ can be arbitrary.

Step 3 Embed
$$\mathcal{N}(\Delta_p) = \frac{1}{a^{2-\kappa}} \int_{\Delta_p} N(x) dx$$

Small particles in Δ_p , where $\cup_p \Delta_p = D$ We assume that $\zeta_m = \frac{h(y_p)}{a^\kappa}$ for all

$$x_m \in \Delta_p$$

The distance between neighboring particles is $d = O\left(a^{\frac{2-\kappa}{3}}\right)$.

Theorem. The resulting new materials has the function $n^2(x)$ as its refraction coefficient with the error which tends to 0 as $a \rightarrow 0$. Accuracy increases as particle size decreases with respect to the wavelength.

Based on formal scattering theory this method allows for the design of a bulk material that has a prescribed refractive index, including negative index values. The material is considered to be a metamaterial but as stated previously does not involve resonant elements in this case. We embed small spheres/particles much smaller than the wavelength into the host medium and we assume these spheres each have a constant refractive index. Distributions of subwavelength-sized structures or “effective medium theories” provide one approach or model to estimate the associated bulk properties of the materials. We assume that the number density of the spheres is known. The host media could be water, or a polymer. A higher density of particles is required for smaller scaled particles in order to agree with the effective medium theory.

3.4 Experimental Application of the Theorem

Table 1: Theoretical steps for finding the concentration of particles required for a given target index.

1	$A_s = \frac{-\zeta S \mu_0}{4\pi}$	Scattering Amplitude and impedance
2	$A_q = \frac{1}{4\pi} k^2 V(n_p^2 - n_o^2)$	Scattering Amplitude and particle index
3	$\zeta = -\frac{k^2}{ S } V(n_p^2 - n_o^2) = \frac{h}{a^\kappa}$	Boundary Impedance
4	$p_1(x) + ip_2(x) = k^2(n_o^2 - n_{target}^2) = 4\pi N(x)h(x)$	Following Ramm's Recipe
5	$N = \frac{N}{a^{2-\kappa}} = \frac{k^2(n_o^2 - n_{target}^2)}{4\pi h(x)a^{2-\kappa}}$	Concentration
6	$N = \frac{k^2(n_o^2 - n_{target}^2)}{4\pi \left(-\frac{k^2 a^\kappa}{ S }\right) V(n_p^2 - n_o^2) a^{2-\kappa}} = \frac{- S (n_o^2 - n_{target}^2)}{4\pi V(n_p^2 - n_o^2) a^2} = \frac{-3(n_o^2 - n_{target}^2)}{4\pi(n_p^2 - n_o^2) a^3}$	Concentration of small inhomogenities
7	$\text{Concentration} = \frac{-3(n_o^2 - n_{target}^2)}{4\pi(n_p^2 - n_o^2) a^3}$	
8	$\text{Concentration} = \frac{-3(n_w^2 - n_{target}^2)}{[4\pi a^3(n_p^2 - n_w^2)]}$	Concentration of inhomogenities required for desired refractive index in water(n_w)

To use the theoretical model for an experimental application we worked through the recipe and derived the concentration of spherical particles necessary for an index of less than unity. There are still numerous obstacles with this derivation such as the need for a singular particle to have an index of less than unity. The other obstacle was determining the point at which the particles (which should be similar in size and shapes)

would touch. Another obstacle is that we needed to consider how this recipe relates to common effective medium theories, and if these theories outperform this recipe?

3.5 Effective Medium Theories

Effective medium theories have been around since the late 1800's. They are a culmination of algebraic formulas that describe the overall permittivity of mainly homogenous inclusions. The effective permittivity of the mixture can be calculated as a function of the constituent's permittivity and their volume fraction. A drawback to these formulas is how they describe inhomogeneous inclusions, which are a challenge. The challenge is calculating the different polarizability of the inclusions.^{80,81}

Maxwell Garnet formula for effective medium is the most common.

$$\varepsilon_{Eff} = \varepsilon_e + 3f\varepsilon_e \frac{\varepsilon_i - \varepsilon_e}{\varepsilon_i + 2\varepsilon_e - f(\varepsilon_i - \varepsilon_e)}$$

Equation 8

Where i is the inclusion and e is the environment. However, as seen in these formulas these are only described restrictions relative to the inclusions and the environments. They provide an upper and lower boundary for the effective permittivities. Overcoming these formulas and describing a more rigorous model for scattering species that have more evolved parameters is somewhat of a limitation.

We concluded that the effective medium theories could only provide us with boundaries based on the values of known indexes. This is limiting because we are trying to induce a resonance response that operates outside these boundaries. We must also consider that for Ramm's model we needed to know the value of the index of the nanoparticle itself, not the bulk index used for mixing formulas. Below are some of the effective medium their bounds we considered in this study.

Wiener Bounds for effective permittivity

Upper Bound

$$\varepsilon_{Eff} = f_1 \varepsilon_1 + f_2 \varepsilon_2$$

Equation 9

Lower Bound

$$\varepsilon_{Eff} = \left(\frac{f_1}{\varepsilon_1} + \frac{f_2}{\varepsilon_2} \right)^{-1}$$

Equation 10

Hashin-Shtrikman Bounds for effective permittivity

Upper Bound where $\varepsilon_1 > \varepsilon_2$

$$\varepsilon_{Eff} = \varepsilon_1 + \frac{f_2}{\frac{1}{\varepsilon_2 - \varepsilon_1} + \frac{f_1}{2\varepsilon_1}}$$

Equation 11

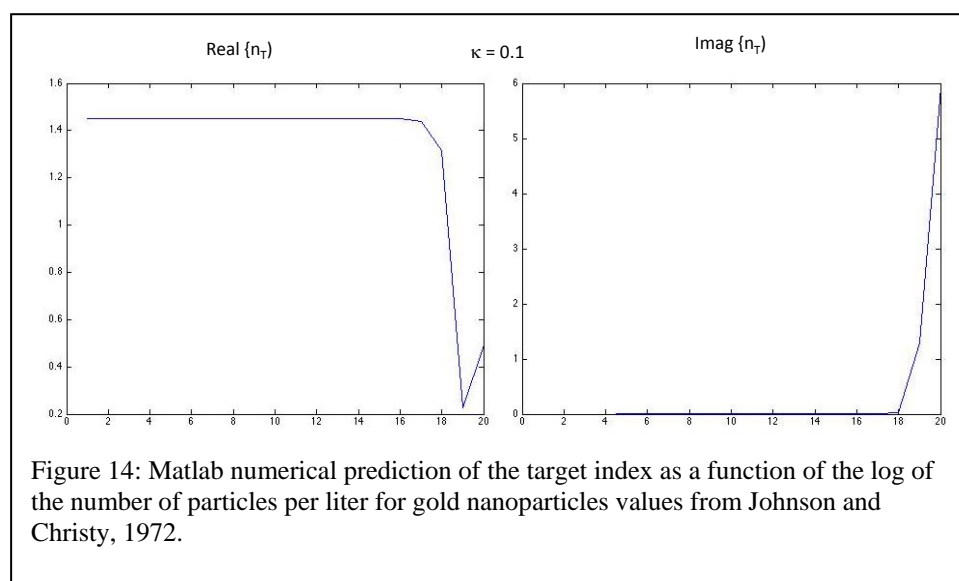
Lower Bound

$$\varepsilon_{Eff} = \varepsilon_2 + \frac{f_1}{\frac{1}{\varepsilon_1 - \varepsilon_2} + \frac{f_2}{2\varepsilon_2}}$$

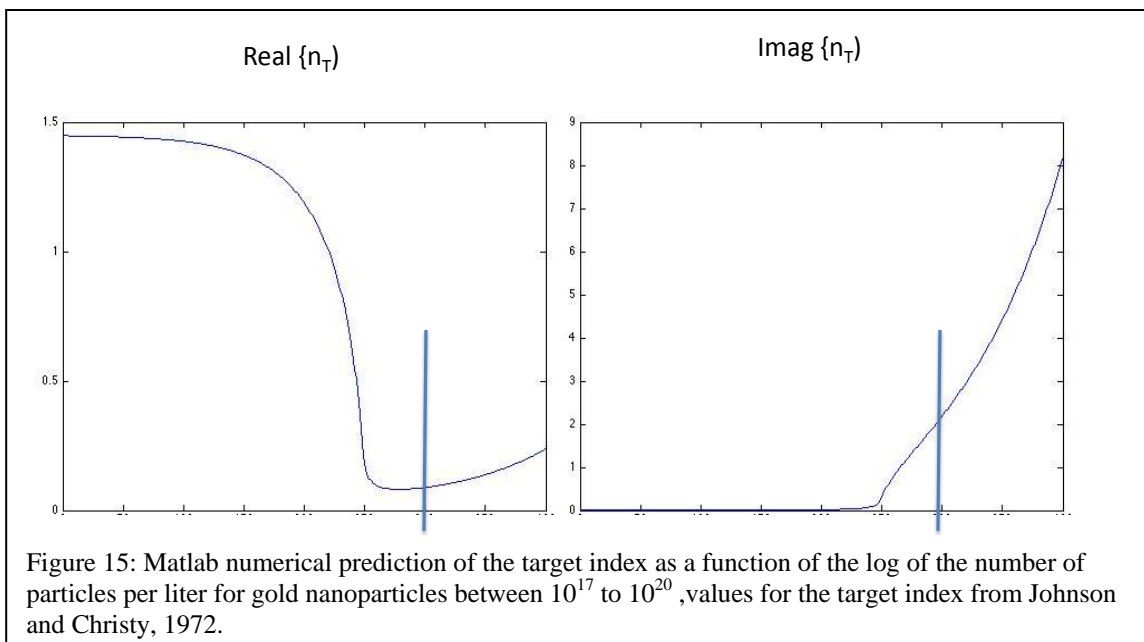
Equation 12

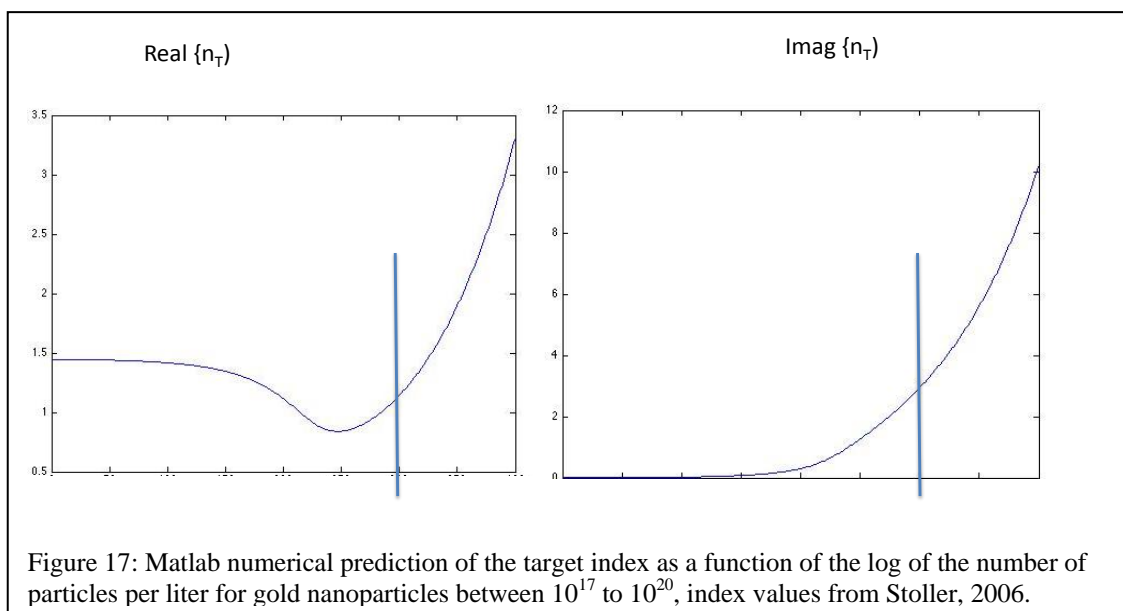
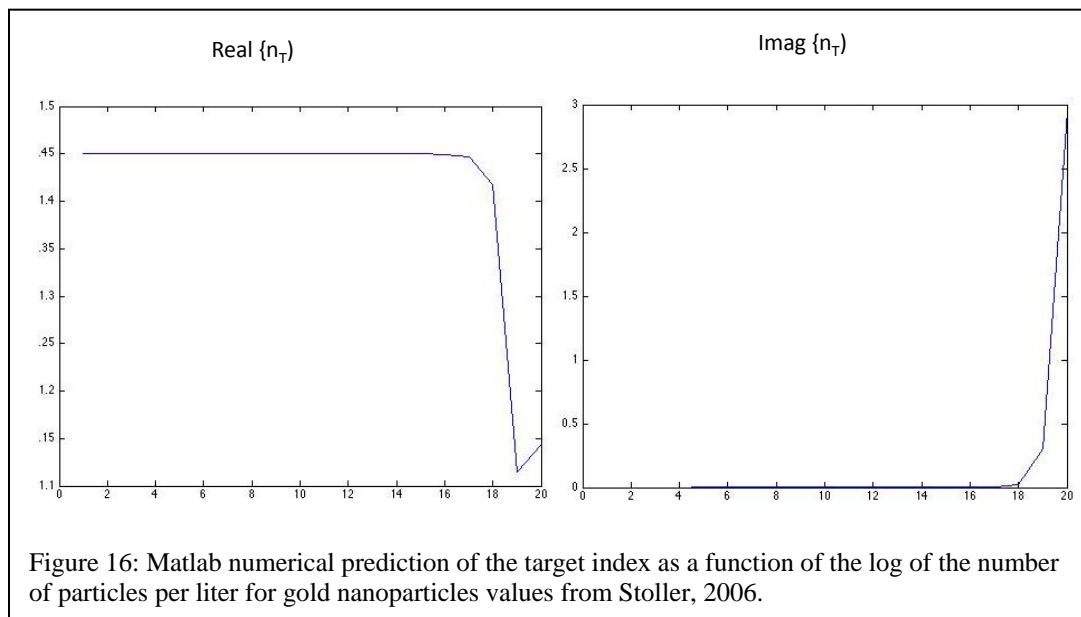
3.6 Numerical construction of Ramm's model

Using Table 1 calculations we created a Matlab code for determining the target index from values for the index of the particle and its loss from the literature. Two values were used, the first was from the experimental data sets of gold thin films from Johnson and Christy. The second values came from experimental data sets of gold nanoparticles 10 nm and 15 nm in radius. In Figures 14 and 16 we determined when a dip in the index occurs from Ramm's theoretical model. In Figure 14 we used as parameters the values for the particle index as $0.29 + i3.01$ taken from the work on gold thin films from Johnson and Christy.²¹ We set as the fitting parameter kappa 0.1. This fitting parameter is left to the experiment to decide its value can be between 0 and 1. We used experimental data from Stoller et al. that concluded that the index for a 15 nm particle was $0.84 + i 1.2$.⁸² We incorporated a ligand into the simulation by assuming that the host material was oleic acid with an index of 1.45.⁸³ Assuming that the particles are face centered cubic the



maximum packing efficiency is 0.74. Therefore the maximum number of particles per liter will be 2.21×10^{19} for a 20 nm particle, in Figures 15 and 17 this limit is shown by a blue line.





We determined that gold nanoparticles were candidates for designing our low loss metamaterial but there are limitations in regards to the loss term. The loss term of the index sky rockets to such a degree from our simulations that the material may not exhibit these required low loss parameters.

We also concluded that the concentration of nanoparticles needed to be at a high degree between 10^{17} to 10^{19} particles/Liter. We also determined that the fitting parameter for both simulations at 0.1 and 0.9 had no variable difference. So, the next question was to determine how can we bring the particles close enough together and still keep a strong scattering response, and what material could be used that had a low loss term?

3.7 Numerical construction of a low loss metamaterial

Before we can begin to fabricate a low loss metamaterial we determined its likelihood by computation simulations using High Frequency Structural Simulations (HFSS). Since, we concluded that the particles needed to be highly concentrated from our Matlab numerical calculations, we verified this factor using HFSS. Gold nanoparticles with a 50 nm radius with variation in particle spacing was simulated. The particles were modeled to be spherical in nature.

In Figure 18 the HFSS model for gold nanoparticles with a 50 nm radius was the second example we had of how controlling particle spacing or particle density could lower the index of the material. In Figure 18, when the gold nanoparticle spacing is reduced, the medium takes on the characteristics of a mirror and the reflectivity of the

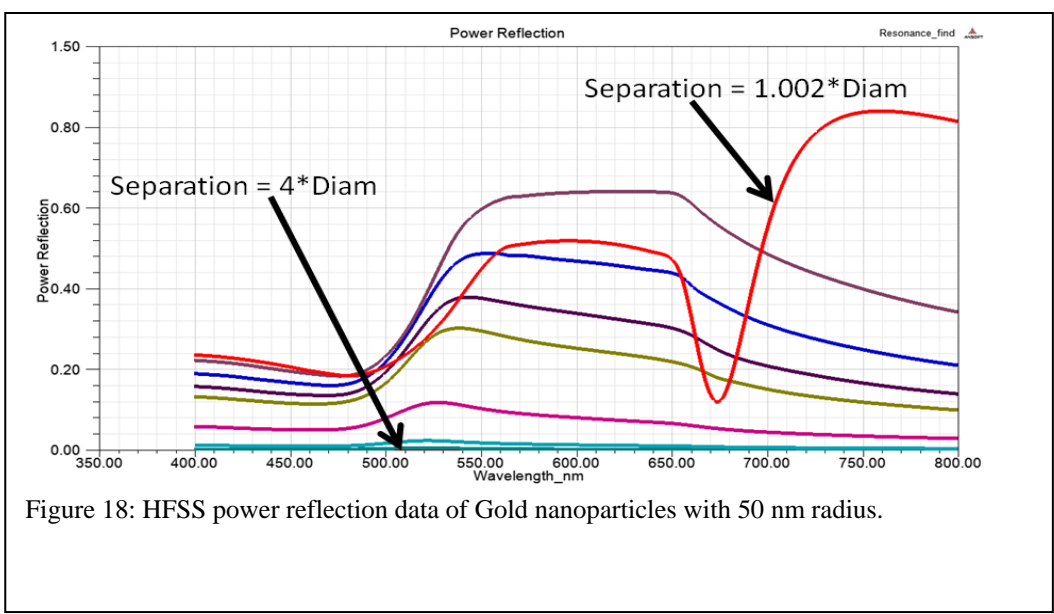


Figure 18: HFSS power reflection data of Gold nanoparticles with 50 nm radius.

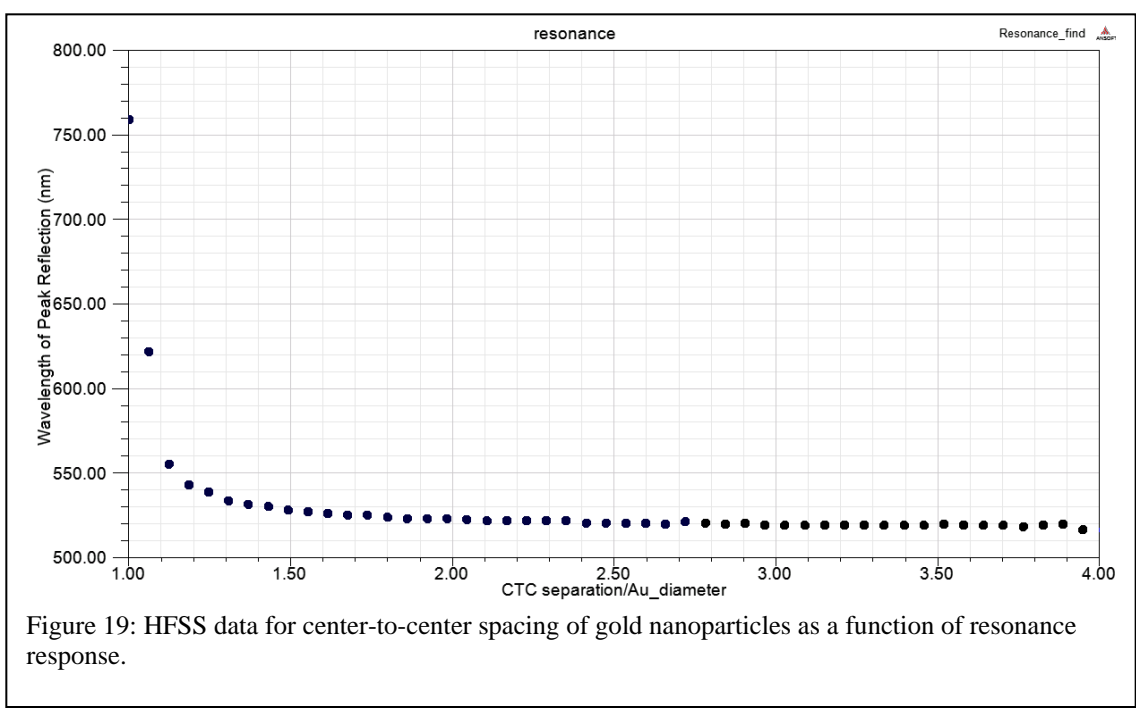


Figure 19: HFSS data for center-to-center spacing of gold nanoparticles as a function of resonance response.

medium increases as shown, however, for certain particle separations, a strongly resonant effect leads to a distinct transmission window. We then became interested in understanding the associated refractive index change that occurs under these circumstances. A coupling effect we determined drives the response.

Figure 19 is a graph further demonstrating the coupling behavior of the resonant gold nanoparticles as the particles become closer and closer together within diameter of each other.

While conducting this research Fontana et al did very similar work with 17nm Au nanoparticles and reported a low index in the visible (red) but with a relatively high loss.⁸⁴ Their findings support this research endeavor and demonstrated that our line of thinking regarding particle proximity is valid.

From the two numerical predictions demonstrated in Matlab and HFSS we still were plagued with finding a material that demonstrated low loss but first we wanted to know more about coupling effects and scattering behaviors of nanoparticles.

3.8 Aluminum Doped ZnO (AZO) a low loss material

The next phase of our design of a low loss metamaterial was to explore what materials in the literature could offer a low loss term. We discovered an article that looked at silver thin films, and zinc oxide thin films doped with aluminum and gallium. In the article they determined that these materials can exhibit a permittivity of less than -1 to -6 between 1000-2000 nm and the loss term from 1000-1500 nm could be less than 0.5.⁸⁵ Using HFSS we calculated numerical predictions of this type of low loss materials and the effect of particle density which incorporates Ramm's theoretical model. We found that it is possible to have an index of less than unity with this type of material. This

effect is prominent in Figure 20 and 21 where we can see the distinctive change in transmission between 1600-1900 nm with increasing particle spacing, and the real part of the index going to less than unity with increasing conductivity. Figure 20, shows that decreasing particle spacing increases scattering between the particles, and the resonant nature of multiple particle interaction, which is a prelude to our hypothesis of quadrupole interactions of the meta-atoms. In Figure 20 the permittivity of the particles was set to -2, this was done to elicit a strong scattering response. If we assumed that the particles are strong scatters then knowing how doping the particle with aluminum affect the index response helps in the design of the nanoparticles. From these data in Figure 20 we concluded that the conductivity of the particle does affect the index, so we decided to use values between 1-6% aluminum.

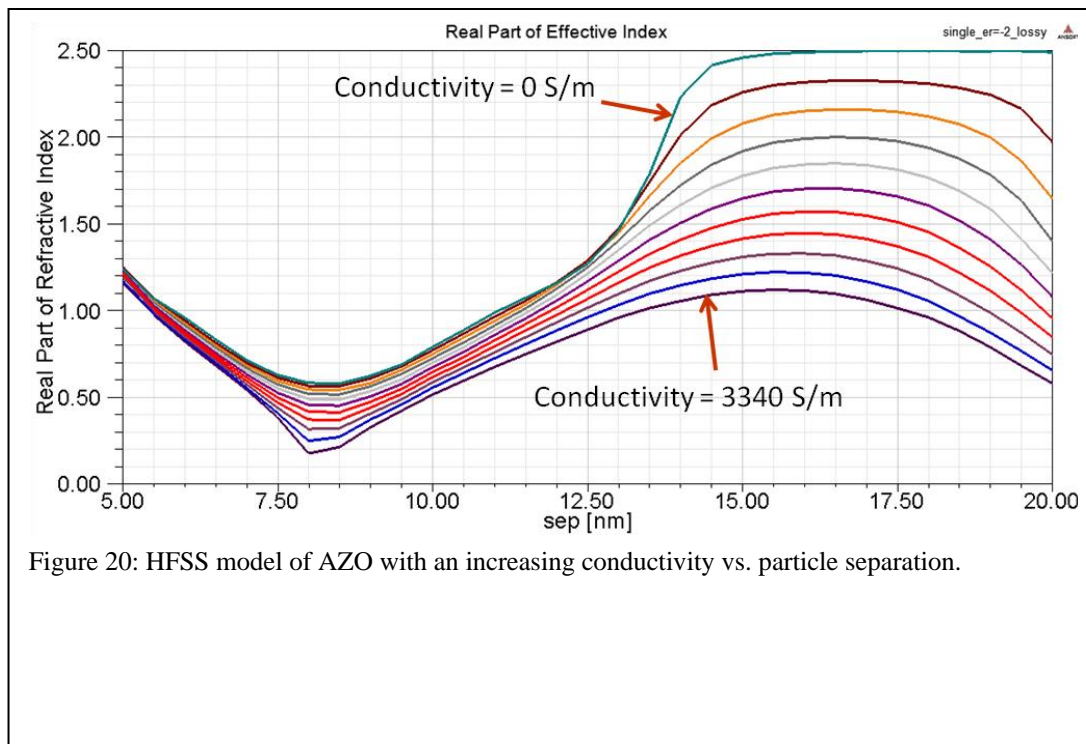
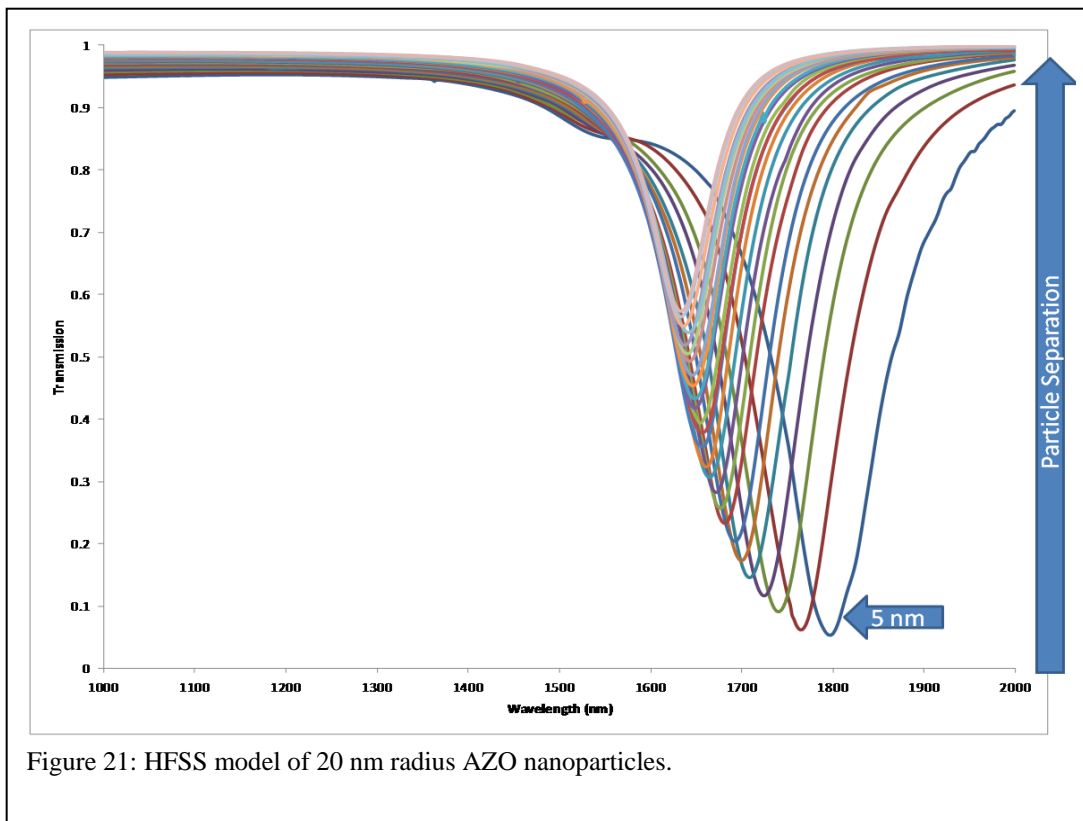


Figure 20: HFSS model of AZO with an increasing conductivity vs. particle separation.

Also, from Figure 21 the scattering response of the particles are the strongest when they are within less than 10 nm for a 20 nm particle. We ran simulations using the permittivity values from the work done by Boltesseva. The radius of the particles ranged from 10-50 nm, and all showed that the spacing of the particles must be less than 10 nm to have a strong scattering response and influence the index.

Finally, we concluded that a transparent conducting oxide such as AZO was the best material to design a low loss metamaterial. So, the next phase is to fabricate AZO nanoparticles and control their spacing with a coating, in this case ligands. The ligands will need to be greater than 1 nm in length. If the particles are spaced greater than 1 nm then we will see a change in the index according to our simulations. To accomplish this ligand coating, we determined that a long aliphatic chain ligand would be required.



CHAPTER IV: RESULTS

4.1 Synthesis of Aluminum Doped Zinc Oxide Nanoparticles

Zinc acetate dihydrate, ACS reagent, $\geq 98\%$ (Sigma-Aldrich), Lithium hydroxide, ACS reagent, $\geq 98.0\%$, (Sigma-Aldrich), Ethanol, Pure, 200 Proof (100%), USP, KOPTEC (VWR), Dodecanethiol, 98% (Sigma-Aldrich), Octadecylamine, 98% (Sigma-Aldrich), Chloroform, ACS, 99.8%, Oleic Acid, (VWR), Hexadecylamine, 90% (VWR).

The synthesis of AZO nanoparticles were carried out using the Sol-gel method described by Spanhel and Anderson.⁶⁸ Although, in their experiment the goal was to obtain colloidal zinc oxide nanoparticles with a diameter of less than 10 nm. Our goal was to fabricate aluminum doped zinc oxide nanoparticles with a size regime of 50-100 nm and with variations of mole percentages of aluminum.

To begin we first took the same mol ratio of inorganic precursors as described by Spanhel and Anderson which was a 1: 1.89 mol ratio of zinc to lithium. The organometallic precursors were carefully weighed to 0.00001 grams. Once the precursors are measured the next step is to disperse them into two separate containers of ethanol. For example, for every 0.5 grams of zinc acetate dihydrate disperse the solute in 25 mL of ethanol. Use the same volume for the dispersion of the lithium hydroxide. The mixtures do not easily disperse in ethanol. To help the solutes to become more

soluble in ethanol vigorous stirring was required. The solutions were stirred at 1100 rpm for one hour or more. The zinc solution was heated to help disperse the solute. The lithium ethanolic solution was stirred vigorously for more than three hours. The next endeavor was to determine how to add or dope the zinc ethanolic solution with aluminum.

Several methods were employed; (1) the aluminum nitrate was added to the zinc acetate dihydrate and both solutes were dispersed in ethanol simultaneously, (2) the aluminum nitrate was dispersed in ethanol and then added sequentially to the zinc ethanolic solution while vigorously stirring. For clarification the zinc acetate dihydrate and aluminum nitrate solutes dispersion in ethanol simultaneously will be known as the water wash method. Also for clarification, the zinc acetate dihydrate and aluminum nitrate solutes dispersed sequentially will be known as the ethanol wash method.

It was found that dispersing a solution of aluminum nitrate into zinc ethanolic solution while heating was the best method, this is the ethanol wash method. This was because there was a limited amount of anhydrous zinc acetate that remained insoluble in the ethanol. With time, the zinc acetate dihydrate does re-crystallize but using this technique it is limited amounts.

Another question to ask is in several publications there is a long period set aside for refluxing the zinc acetate ethanolic solution, anywhere from 1-24 hours. Since we want to keep this as simple and straightforward as possible, we looked at the benefits of doing this long reflux. According to the work by Meulenkamp the same particles can be achieved without this long refluxing period.⁸⁶ What is critical is the pH of the base (lithium hydroxide) and the amount of water that is inadvertently always a part of your

zinc ethanolic solution. If there is an overabundance of water in your solution then the material will cause the colloids to aggregate and higher rates. This reaction rate may be too high to adequately compensate for during the synthesis.

To compromise for this refluxing period, we refluxed the zinc ethanolic solution for 15 minutes and let the solution cool to room temperature and chilled to 15 °C.

The solution was chilled to suppress particle growth due to the unknown water content in the solution and the effect of the aluminum on particle growth as well.

Once all of the solutions are complete, they were added at a controlled rate. The lithium hydroxide was added to the zinc-aluminum solution drop wise at a rate of 3 mL/min. It should be noted that to increase the amount of product the recipe was tripled. To have the particles be as monodispersed as possible the stir rate was controlled at 1100 rpm and the drop rate remained steady.

Chilling the zinc-aluminum solution slowed the aggregation of the nanoparticles. Within 45 minutes the solution had a bluish hue and with time became more opaque and whitish. UV-VIS spectroscopy was employed to help monitor the formation of the particles and control the growth. The percentages of aluminum were 1, 3, and 6 mole percent in relationship to zinc.

Quenching particle growth is difficult since there is an excess amount of reducing agent in the form of the lithium hydroxide and water in the solution. The particles were quenched by centrifuge for 3 minutes at 6500 rpm. Two methods were used to remove the excess amount of reducing agent. The first was to only centrifuge the nanoparticles and remove the supernate and re-disperse in ethanol and re-centrifuge. This is called the Ethanol Wash Method. The second method was to add water to the nanoparticles. In this

synthesis 50 mL of water was added and then the particles were centrifuged. This is called the Water Wash Method. Upon the addition of the water the rate of aggregation increased and the solution quickly became opaque and white. The size of all three types of nanoparticles was monitored with UV-VIS spectroscopy (Figures 22 and 23), Fluorimetry (Figures (27 and 26) and Dynamic Light Scattering. (Figures 24-26)

Table 2: UV-VIS spectrograph measured data from the Al-Doped ZnO during synthesis using the ethanol wash method.

AZO-Ethanol Wash Synthesis	Maximum Peak	Normalized Maximum Peak	Wavelength (nm)	Difference in Wavelength (nm)	Shift in Wavelength	% Difference in Absorbance
1% Al-Doped 30 min	0.96	0.33	314			
1% Al-Doped 45min	2.47	0.85	320	6	Red Shift	22%
3% Al-Doped 30 min	2.43	0.84	309	0	None	0
6% Al-Doped 30 min	1.41	0.48	311			
6% Al-Doped 45 min	2.91	1.00	297	2	Red Shift	17%
6% Al-Doped centrifuge supernate	0.46	0.16	332	35	Red Shift	25%

4.2 Monitoring Particle Growth

One of the characterization techniques to monitor particle growth was done using UV-VIS spectroscopy. AZO colloids will have an absorbance peak in the ultra-violet region of the electromagnetic spectrum. Therefore, with trial and error we set growth time based on previously observed UV-VIS spectrographs for 50-150 nm AZO colloids. From this known region if the peaks shifted in wavelengths or the absorbance increased it was clear whether or not to increase the reaction time or halt the particle growth. As seen in Figure 22 and 23, the shift of the peaks into the red of the electromagnetic spectrum is indicative of particle aggregation or growth. From the data it is clear that growth of the nanoparticles occurs very rapidly and that the next stage is to halt the particle formation.

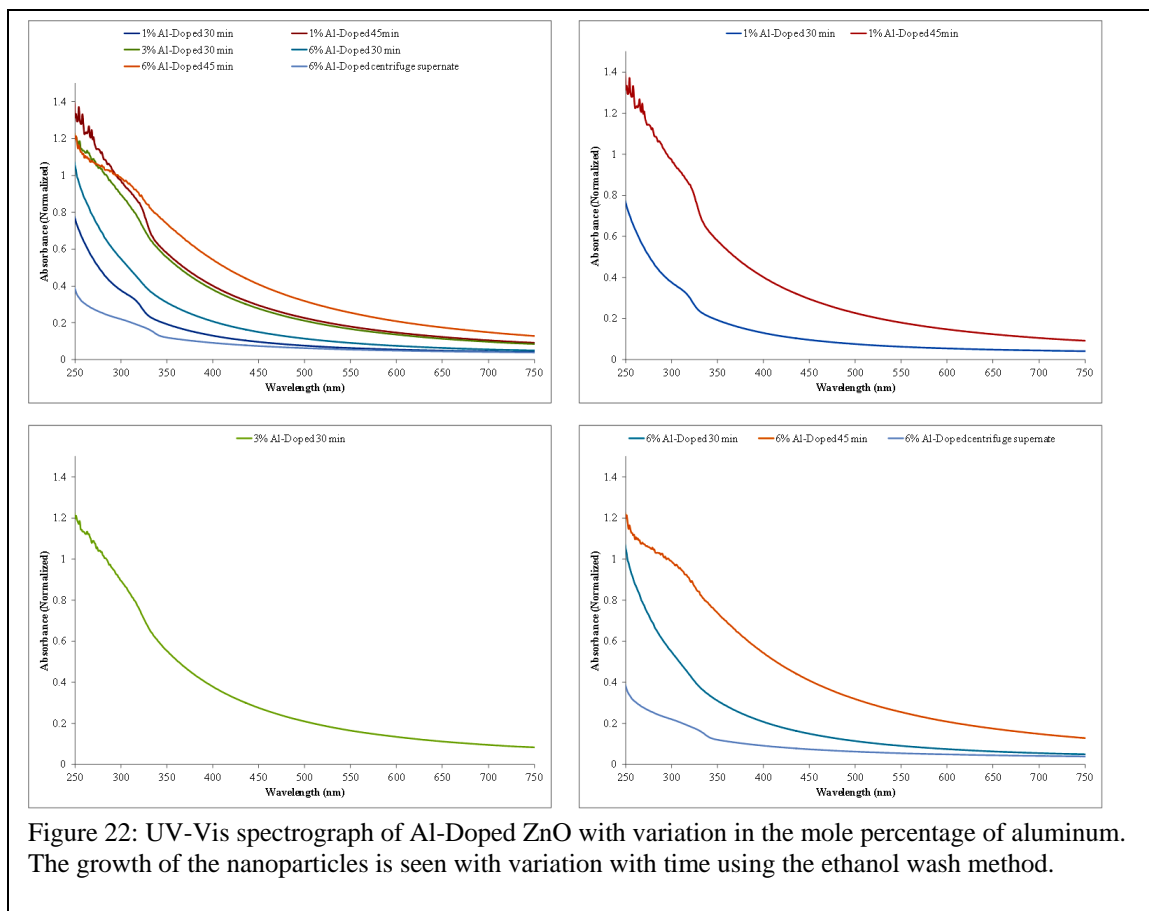


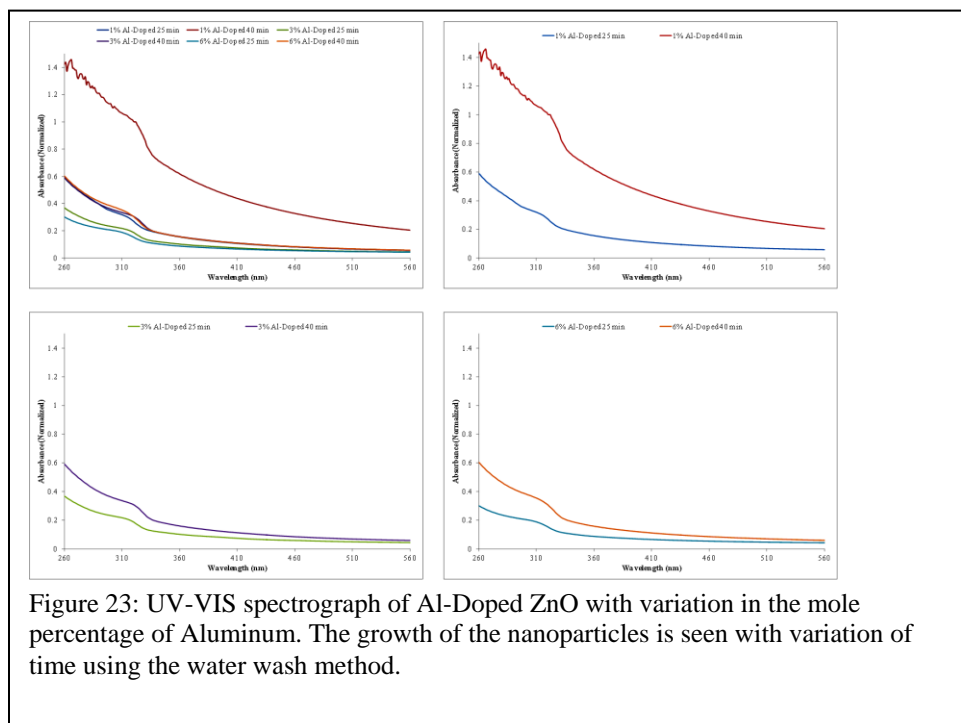
Figure 22: UV-Vis spectrograph of Al-Doped ZnO with variation in the mole percentage of aluminum. The growth of the nanoparticles is seen with variation with time using the ethanol wash method.

In Figure 22, the percent difference in the peak absorbance is relatively the same for all the different percentages of aluminum dopants for the ethanol wash method. There was no definitive distinction between the amount of aluminum added and the rate of growth according to the UV-VIS spectrographs. However, what was clear was the time required for the reaction was to take place. This conclusion was verified by dynamic light scattering to quantify the particle size. (Figures 24-26, Table 4) The growth time for 1% and 6% AZO was 40 minutes to reach similar UV-VIS peaks and diameters according to DLS data. For the 3% the growth rate was stopped at 30 minutes because the peaks were similar to the 40 minute peak for the 1% AZO and the diameter was nearing 150 nm.

For the water wash method particle growth was fairly controlled within 50-150 nm. The exception is in the case of the 1% Al-Doped ZnO colloids. The UV-VIS shows a peak absorbance (Figure 23) that is substantially greater than the other colloids. The size of the colloids after 40 minutes was 385 nm in diameter. The reason for this growth is that there may have been a change in the drop rate of the lithium hydroxide into the zinc-aluminum ethanolic solution. If the rate increased this would cause the reaction rate to increase and thus colloid growth will extend beyond those boundaries of 50-150 nm in diameter

Table 3: UV-VIS spectrograph measured data from the Al-Doped ZnO during synthesis using the water wash method.

AZO-Water Wash Synthesis	Maximum Peak	Normalized Maximum Peak	Wavelength (nm)	Difference in Wavelength (nm)	Shift in Wavelength	% Difference in Absorbance
1% Al-Doped 25 min	0.84	0.31	312			
1% Al-Doped 40 min	2.69	1.00	321	9	Red Shift	26%
3% Al-Doped 25 min	0.56	0.21	314			
3% Al-Doped 40 min	0.85	0.31	318	4	Red Shift	10%
6% Al-Doped 25 min	0.46	0.17	315			
6% Al-Doped 40 min	0.88	0.33	316	1	Red Shift	15%



To characterize the size of the nanoparticles in relationship to our parameters of reaction time, and the amount of dopant we used dynamic light scattering (DLS). The DLS data showed that using the ethanol wash method (Figures 24-26) controlled the particle size with a difference of less than 10% within a reaction time of 45 minutes. The

water wash method shows that the colloid growth is more rapid, the difference in particle size with time was greater than 19%. (Table 5) For the water wash, as the solutes dispersed in the ethanol in the initial states of the synthesis formation of anhydrous zinc acetate was more abundant than ethanol wash method. This caused the reaction to be slowed and thus the variation in the diameters with time.

The goal is to have an aluminum doped zinc oxide nanoparticles that is 50-100 nm in diameter. By using the DLS we determined the proper reactionary period for achieving this goal. The ethanol only wash was the best method to control the size of the nanoparticles because there was little variation in size between 30-45 min of the reaction period.

Table 4: Dynamic Light Scattering measured data of Al-Doped ZnO during synthesis in relationship to particle growth using the ethanol wash method.

AZO Ethanol Wash Synthesis	Mean Diameter	Polydispersity	% Difference in Diameter
1%-30 min	78	0.241	
1%-45 min	97	0.319	5%
3%-30 min	131	0.361	0%
6%-30 min	106	0.297	
6%-45 min	159	0.289	10%
6%-Supernate	131	0.237	5%

Table 5: Dynamic Light Scattering measured data of Al-Doped ZnO during synthesis in relationship to particle growth using the water wash method.

AZO Water Wash Synthesis	Mean Diameter	Polydispersity	% Difference in Diameter
1%-25 min	56	18%	37%
1%-40 min	385	25%	
3%-25 min	19	22%	35%
3%-40 min	108	20%	
6%-25 min	60	20%	19%
6%-40 min	134	24%	

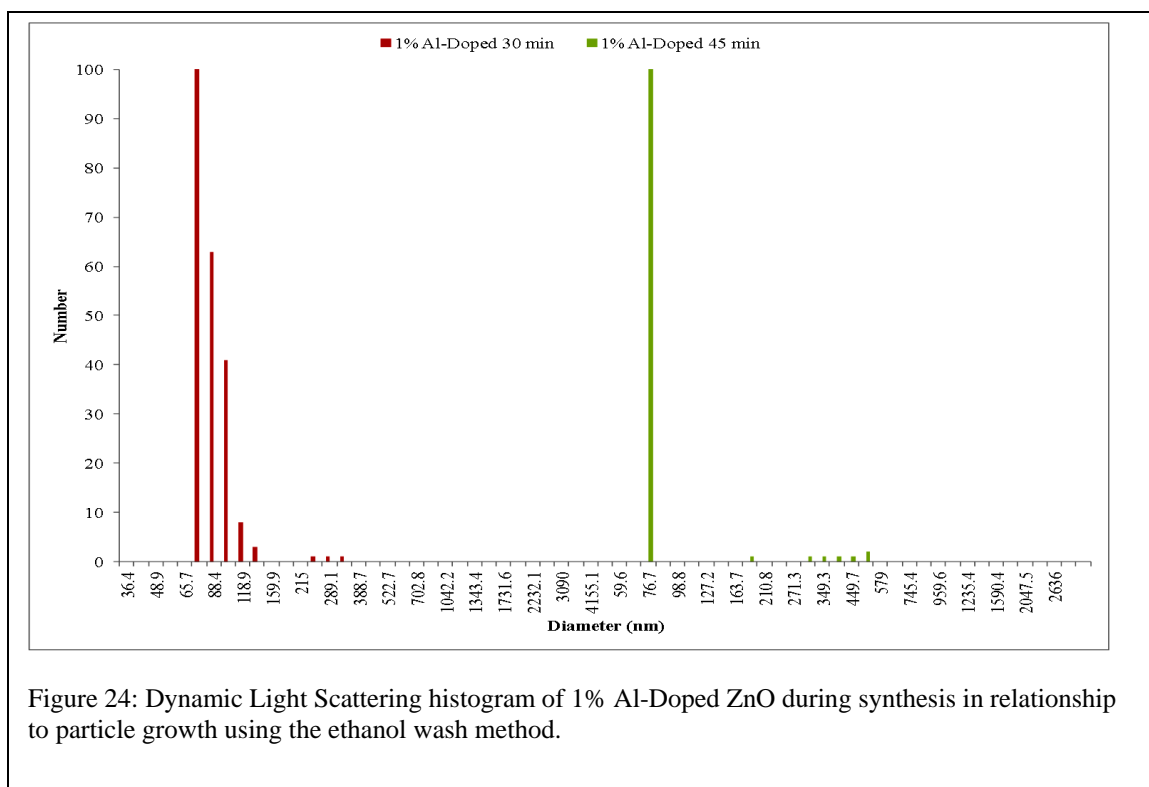
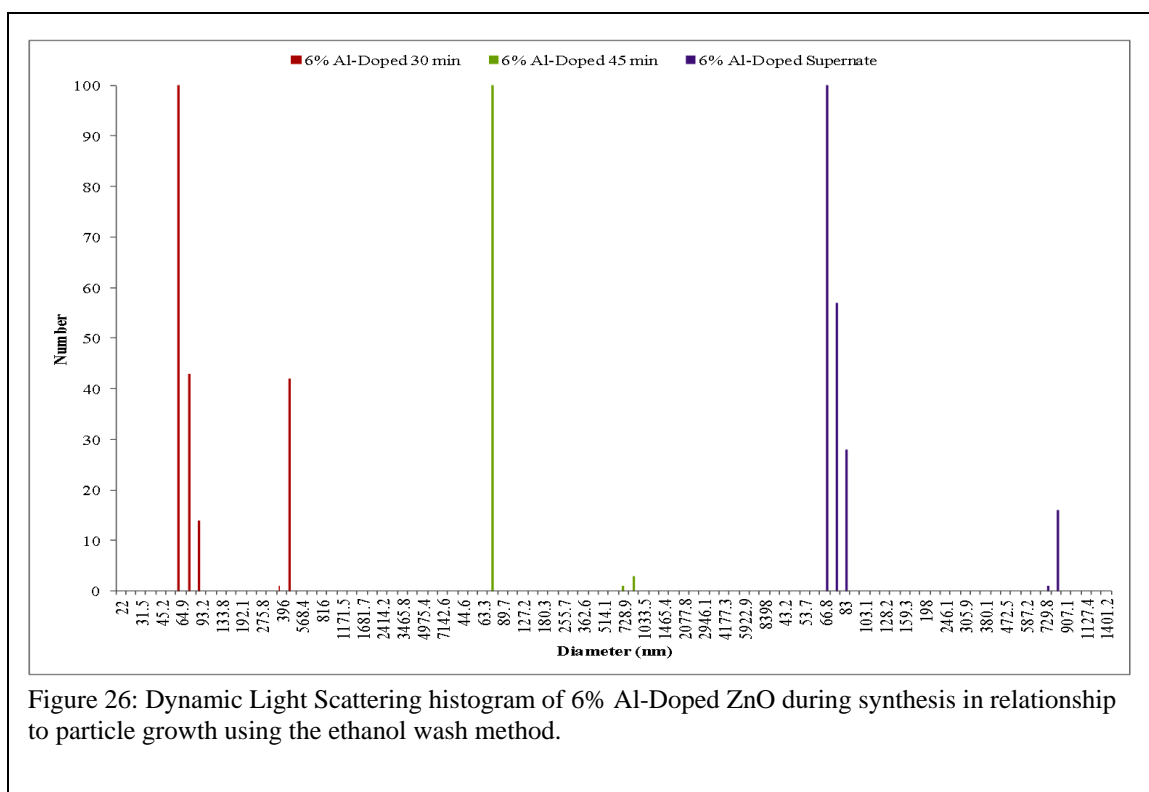
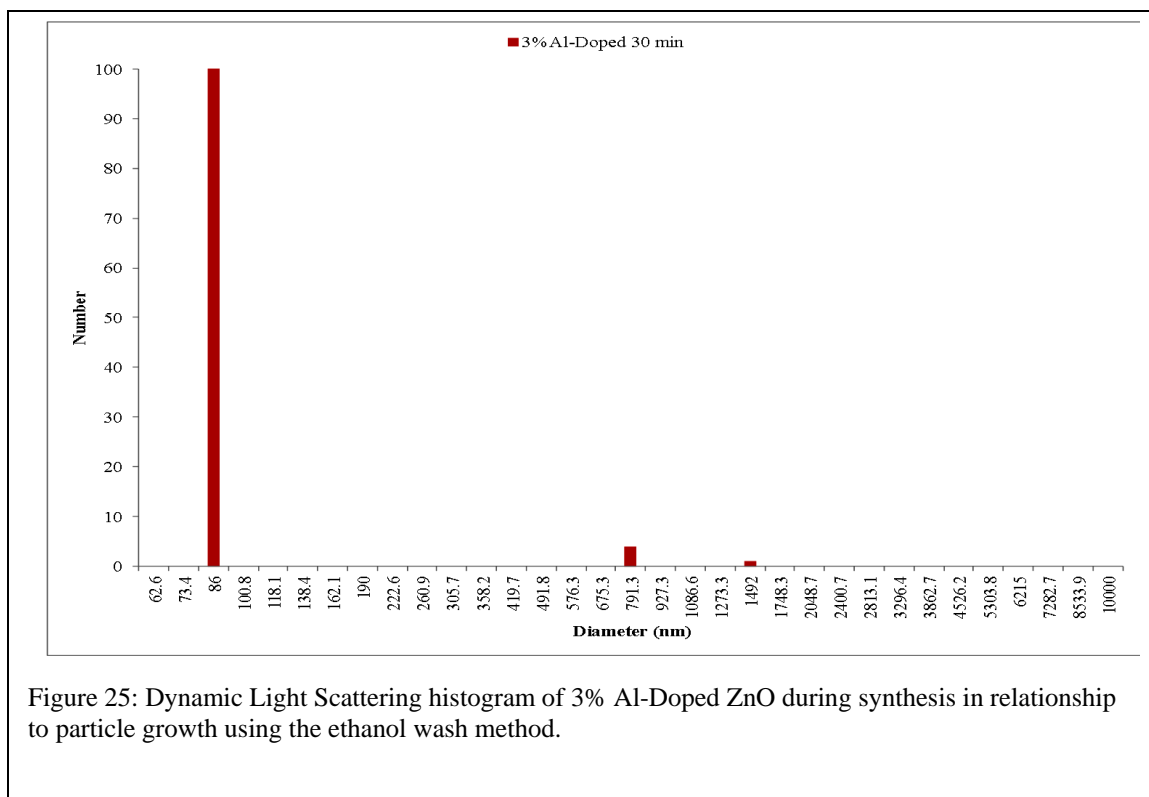


Figure 24: Dynamic Light Scattering histogram of 1% Al-Doped ZnO during synthesis in relationship to particle growth using the ethanol wash method.



Another way to characterize the synthesis of AZO nanoparticles was done by monitoring the emission peaks of the AZO sols. ZnO colloids have an emission between 500 and 600 nm. Therefore, this characterization method is an excellent check to determine if the synthesis is going well. Also, we can look at the effect of the aluminum as an n-dopant to determine if the emission intensity diminishes or improves with the percentage of aluminum. For the ethanol wash method, in Figure 27 we can see how the emission is diminished and is slightly shifting into the red with increasing aluminum concentration. The emission peaks are between 500-569 nm and the intensity decreases with increased percentages of aluminum for the ethanol wash. The only difference between the ethanol method and the water method at this stage of growth of colloids is the method of aluminum doping. What was interesting was the diminishing of the emission spectra for the ethanol wash relative to percentage of aluminum. It is unclear why there is a difference in the emission spectra for the two methods. So, the question is what would cause the emissions to reduce with increasing concentration of aluminum.

We know that emissions of molecules can be affected by such things as temperature, pH, solvents, and molecular oxygen and transition metals. We also know that aluminum is a paramagnetic element like molecular oxygen. Is it plausible that there is Al_2O_3 within the reaction vessel at this point of the synthesis with increased concentration of aluminum, and this may have caused the decreased in the emissions. However, if this was the case it would be present in the water wash method. The cause for the diminishing of the emission spectra for the ethanol wash method is still unclear at this point. Table 6 and 7 gives the experimental data collected from the fluorimeter.

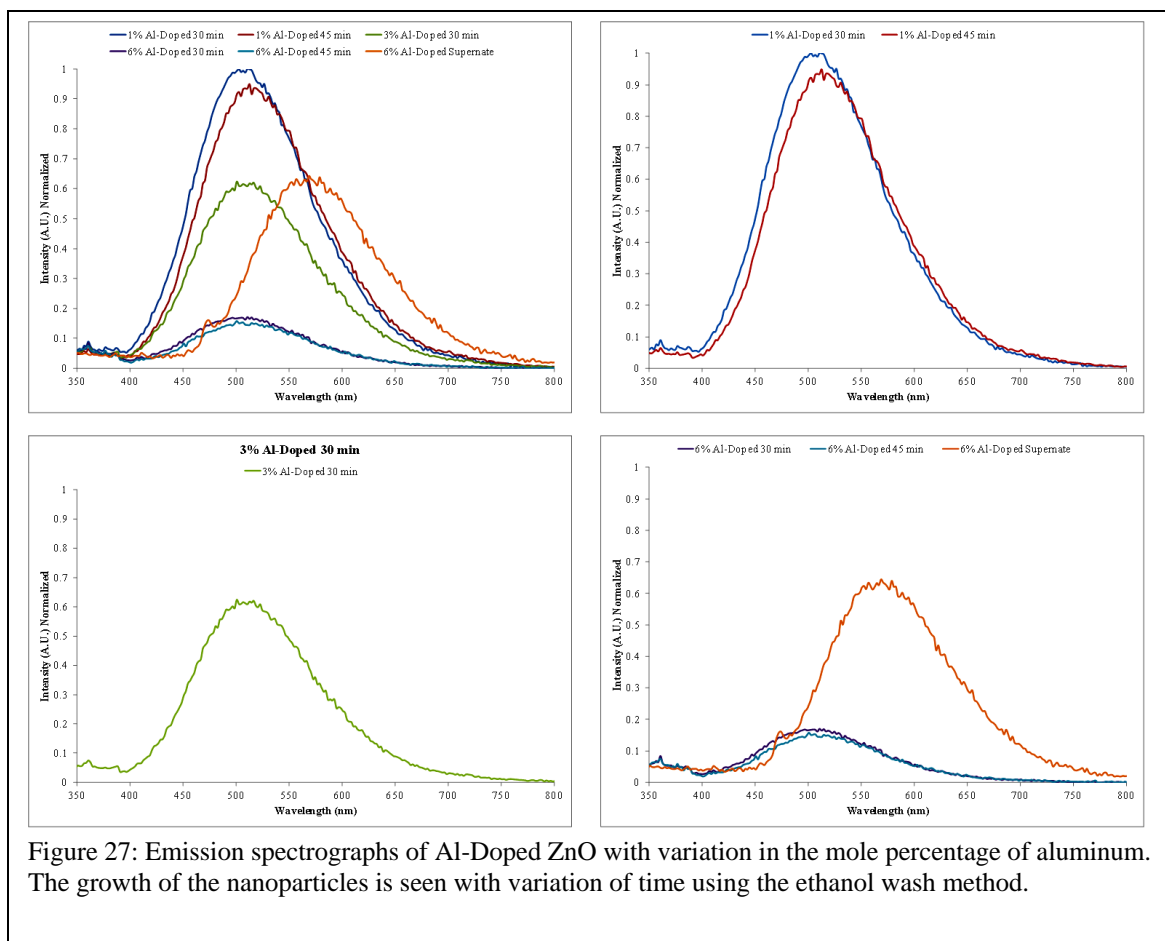


Table 6: Emission spectrograph measured data from the Al-Doped ZnO during synthesis using the ethanol only wash method.

AZO Ethanol Wash Synthesis	Maximum Peak	Normalized Maximum Peak	Wavelength (nm)	Difference in Wavelength (nm)	Shift in Wavelength	% Difference in Intensity (A.U)
1%-30 min	37.51	1.00	510.9	2	Red Shift	1%
1%-45 min	35.58	0.95	513.0			
3%-30 min	23.42	0.62	516.9	0	None Available	None Available
6%-30 min	6.40	0.17	510.9	-10	Blue Shift	2%
6%-45 min	5.93	0.16	500.9			
6%-Supernate	24.14	0.64	569.0	58	Red Shift	29%

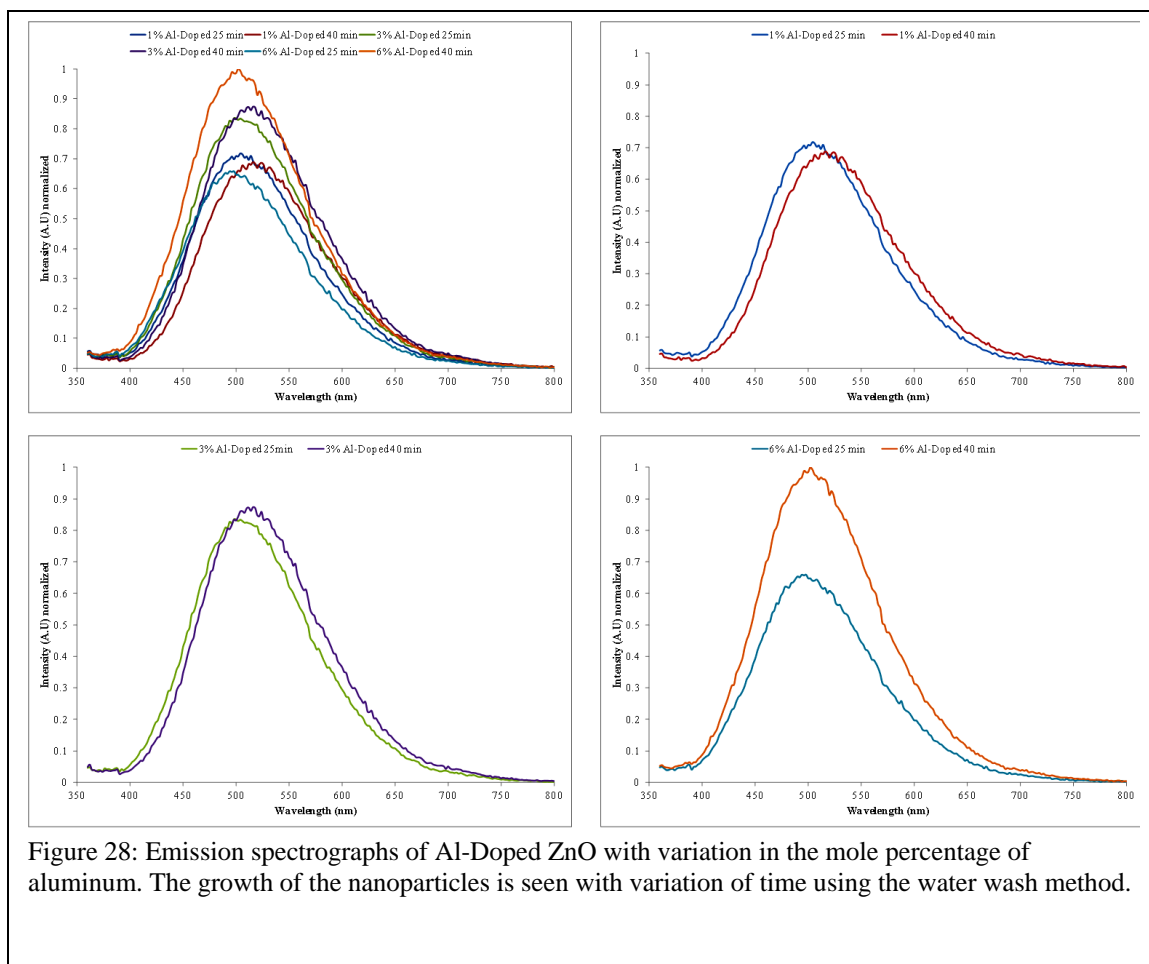
The fluorescence data from the water wash method is not the same trend as the ethanol wash method. The emission peaks are between 498-516 nm and the intensity of

emission peaks slightly increase with increasing reaction time. The wavelengths for the emission are consistent with the literature. Therefore, despite some interesting phenomenon both method of synthesis show the same emission regions. The conclusion is that AZO colloids are present for both types of methods and the characterization supports colloids between 50-150 nm in diameter.

However, the material is still a sol-gel at this stage and a more definitive conclusion can be drawn once the nanoparticles have been calcinated.

Table 7: Emission spectrograph measured data from the Al-Doped ZnO during synthesis using the water wash method.

AZO Water Wash Synthesis	Maximum Peak	Normalized Maximum Peak	Wavelength (nm)	Difference in Wavelength (nm)	Shift in Wavelength	% Difference in Intensity (A.U)
1%-25 min	39.55	0.72	504	12	Red Shift	1%
1%-40 min	37.99	0.69	516			
3%-25 min	46.03	0.83	498	18	Red Shift	1%
3%-40 min	48.21	0.87	516			
6%-25 min	36.35	0.66	498	4	Red Shift	10%
6%-40 min	55.13	1.00	502			



4.3 Formation of AZO powders

The final stage of the synthesis after centrifugation is calcinations of the AZO nanoparticles by a vacuum oven. The nanoparticles were placed in at 65°C for 2 hours. During that time the nanoparticles became like a clear crystal. The nanoparticles were removed from the oven and placed in another over under ambient air for 15 minutes at 120°C. After heating in the oven under ambient air the nanoparticles became as a white powder and were ground with a mortar and pestle into a fine powder. Several trials were done to find the correct temperature and time to calcinate the powders. If the particles

were heated for too long a period of time and at a higher temperature then the result would be clear crystals. Another, noticeable difference in the powders where when the particles were microns in diameter the result would be white flakes.

In conclusion, the synthesis of AZO nanoparticles was straightforward. However, many trials were done to control the growth rate of the nanoparticles. Both synthetic methods yield a large quantity of product roughly 60% yield. The ethanol wash method is favored due to the fact that growth of the nanoparticles was slower. It is believed that the addition of aluminum ethanolic solution helped control the size of the nanoparticles. Even within a 45 minute time frame the particle growth was more controlled.

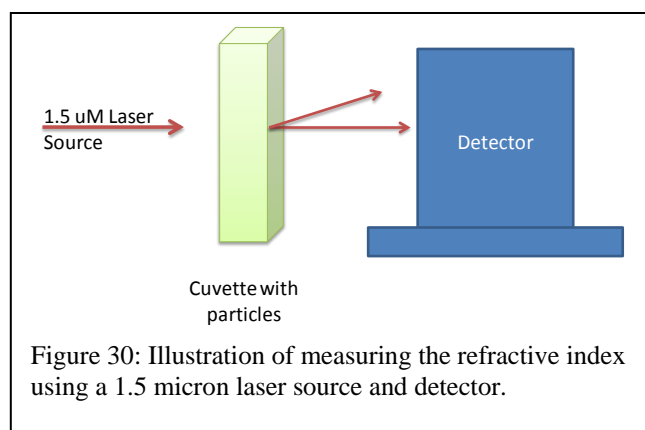
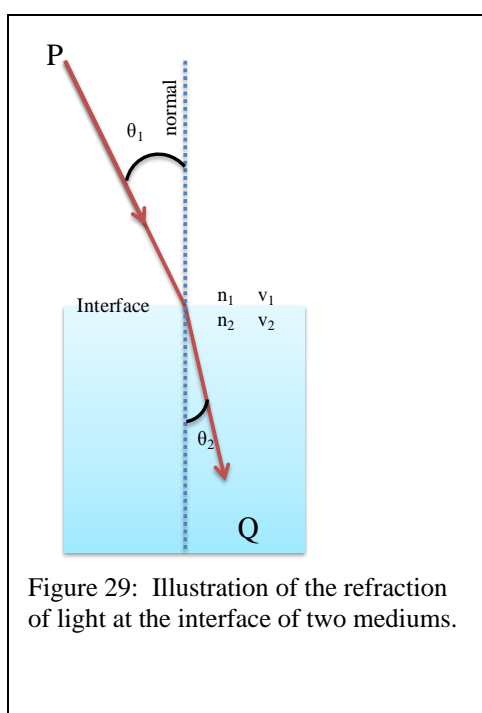
4.4 Constructing the Low Loss Metamaterial

Once the synthetic procedure for AZO nanoparticles was developed the next step was to adhere to the following research goals congruently.

- 1) Prepare different concentrations of these particles in a transparent host and compare measured index values with theory.
- 2) Determine the effect of coatings (e.g. ligands) on measured surface boundary impedance values.
- 3) Develop bulk materials with increasing particle concentrations to approach an index close to zero (useful for many applications by exploiting form-birefringence).

To incorporate the scattering phenomenon of particles with proximity of less than 10 nm, we strategized how to accomplish this goal. The particles in air will touch each other and be highly concentrated so it might be said that this would lead to an index of less than one according to our simulation data. But the material must be greater than a few nanometers from particle to particle. The question is can we suspend the AZO

nanoparticles in a transparent host and measure the index values with theory. We tried a back of the mill approach to this using purchased ZnO nanoparticles that were doped with 6% aluminum. We placed roughly a gram of nanoparticles in a 1 cm plastic cuvette and measured the index with a laser. The idea was to change the position and angle of the cuvette and measure the refractive index of the nanoparticles using Snell's law.



$$\frac{\sin\theta_1}{\sin\theta_2} = \frac{n_2}{n_1}$$

Equation 13

Unfortunately, the particle density was too strongly attenuating for reliable measurements. This led to the idea to distribute the particles on a thin film and measure

the index of refraction. There is extensive literary research involving AZO thin films and their method of fabrication is mainly some form of laser ablation or chemical vapor deposition. However, the use of AZO spherical nanoparticles in this capacity is not widely explored.

4.5 Controlling the assembly of AZO nanoparticles

We tried several methods to adhere the ligands onto the surface. We tried to incorporate the ligand into the initial stages of the synthesis of AZO nanoparticles. In the case for dodecanethiol we found that there were too many side reactions that were taking place for proper particle formation. The dodecanethiol and the lithium hydroxide would react separately and a milk white powder would be the result. This product was without the inclusion of zinc precursor.

We also tried to sonicate the zinc precursor in ethanol with hexadecylamine without the lithium hydroxide, however the precipitate that resulted when dried was flaky and the size was larger than a micron and it was polydispersed.

From these methods it was decided that the best method to adhere ligands onto the surface without aggregating the particles to a substantial degree would be adhesion after AZO nanoparticles synthesis.

To adhere the ligand onto the surface of the AZO nanoparticles, they were suspended in chloroform and then the ligand was added and stirred at 700 rpm for a time determined by the type of ligand.

We will now focus our attention on the results of our method for adsorbing organic ligands onto the surface of AZO nanoparticles.

AZO nanoparticles were coated with several types of organic ligands; oleic acid, hexadecylamine (HDA), dodecanethiol (DDT) and octadecylamine (ODA). The -SH, -NH₂, and COOH functional groups of these ligands were expected to adsorb onto the surface of the AZO nanoparticles. We studied the surface adhesion using Infrared spectroscopy and particle growth using dynamic light scattering and UV-VIS spectroscopy. We hypothesized that the ligand surrounding the nanoparticles would allow for the adequate spacing between nanoparticles which would create the desired scattering phenomenon.

The ratios of nanoparticles to ligand was altered during the course of our experimental study, but we found that using 0.08-0.1 grams of AZO to 50 μ L of oleic acid (OA), 500 μ L of a 0.3g in 10 mL chloroform solution octadecylamine (ODA), and 0.004 g of hexadecylamine (HDA). The amount of AZO did not necessarily need to be exact because as we observed once these ligands were adhered to the surface the particles the particles dispersion in chloroform would increase. We also studied the time to adhere the ligands onto the surface of the nanoparticles. This ranged from 14-34 hours depending on the ligand. We determined that octadecylamine with an adhesion time of 24 hours or more was the best ligand for our fabrication needs.

AZO ethanol wash data sets were the focus for creating a low loss metamaterial. The experimental data demonstrated that the polydispersity of the original AZO nanoparticles before being coated with an organic ligand became monodispersed also the particle size decreases substantially. This is because the large surface area of the AZO nanoparticles. Some of the particles ranged in size from 87-706 nm before surface adhesion of the organic ligand according to Table 8 and Figure 31.

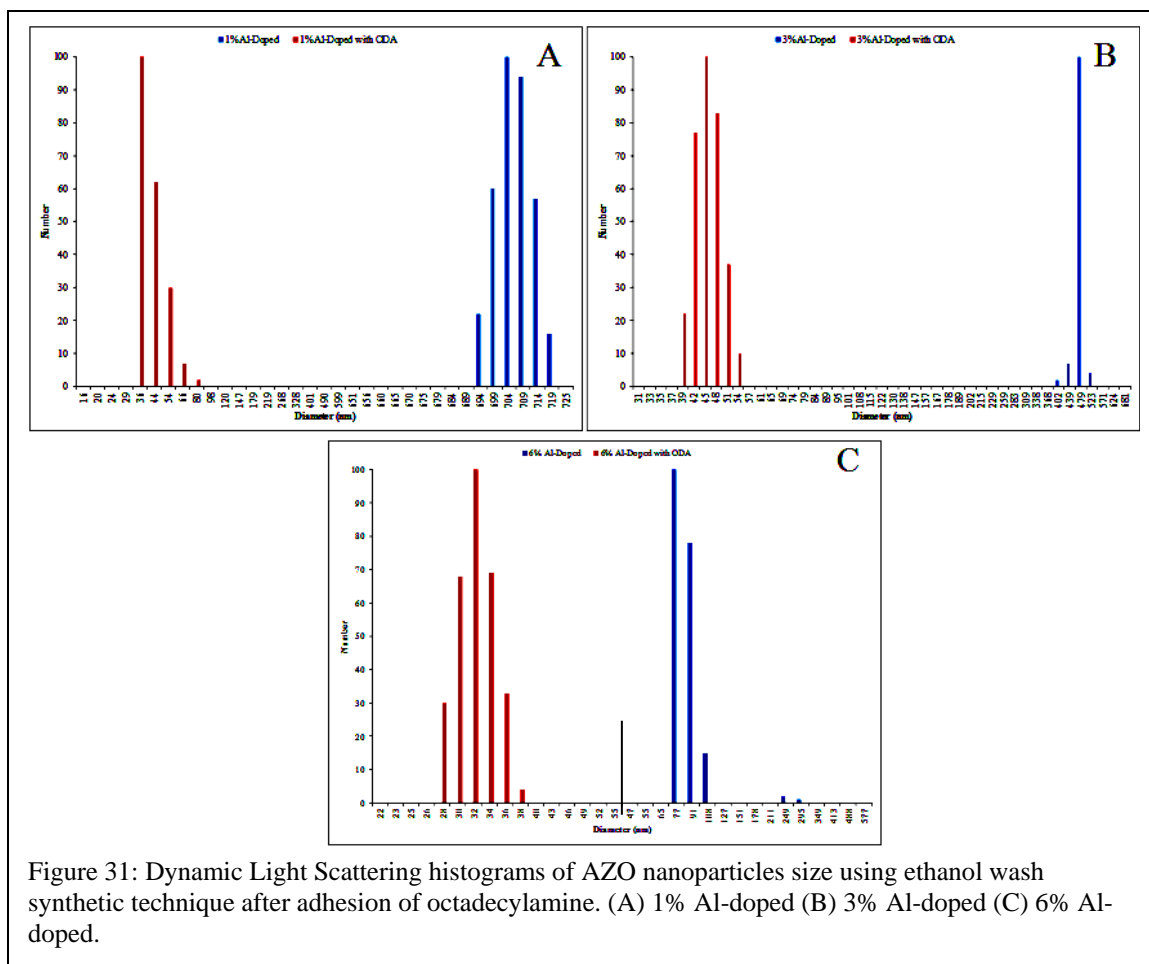


Figure 31: Dynamic Light Scattering histograms of AZO nanoparticles size using ethanol wash synthetic technique after adhesion of octadecylamine. (A) 1% Al-doped (B) 3% Al-doped (C) 6% Al-doped.

It can be stated that it is possible to use a higher concentration of ligands for surface adhesion, and this is something that can be explored further in the future.

Table 8: Size of AZO nanoparticles using ethanol wash synthetic technique after adhesion of octadecylamine.

AZO Ethanol Wash Ligand Study	Mean Diameter	Polydispersity	% Difference in Diameter
1% Al-Doped	706	13.6%	44%
1% Al-Doped with ODA	43	27.4%	
3% Al-Doped	482	32.3%	41%
3% Al-Doped with ODA	45	24.4%	
6% Al-Doped	87	26.2%	23%
6% Al-Doped with ODA	32	21.7%	

The UV-VIS spectrographs shown in Figure 32 demonstrate the amazing increased band gap and prominent peaks after adhesion of the ligand. One must keep in mind that all of the particles were dispersed in chloroform and AZO nanoparticles before ligand adhesion does not disperse well in chloroform. Nonetheless, the peaks show a shelf like property which is indicative of AZO nanoparticles. It can also be said that the peak maxima is dependent on the percentage of aluminum within the nanoparticles. As the concentration of aluminum increases this changes the carrier concentration and the results is a broadening of the band gap which is consistent with the literature.⁸⁷⁻⁹⁰

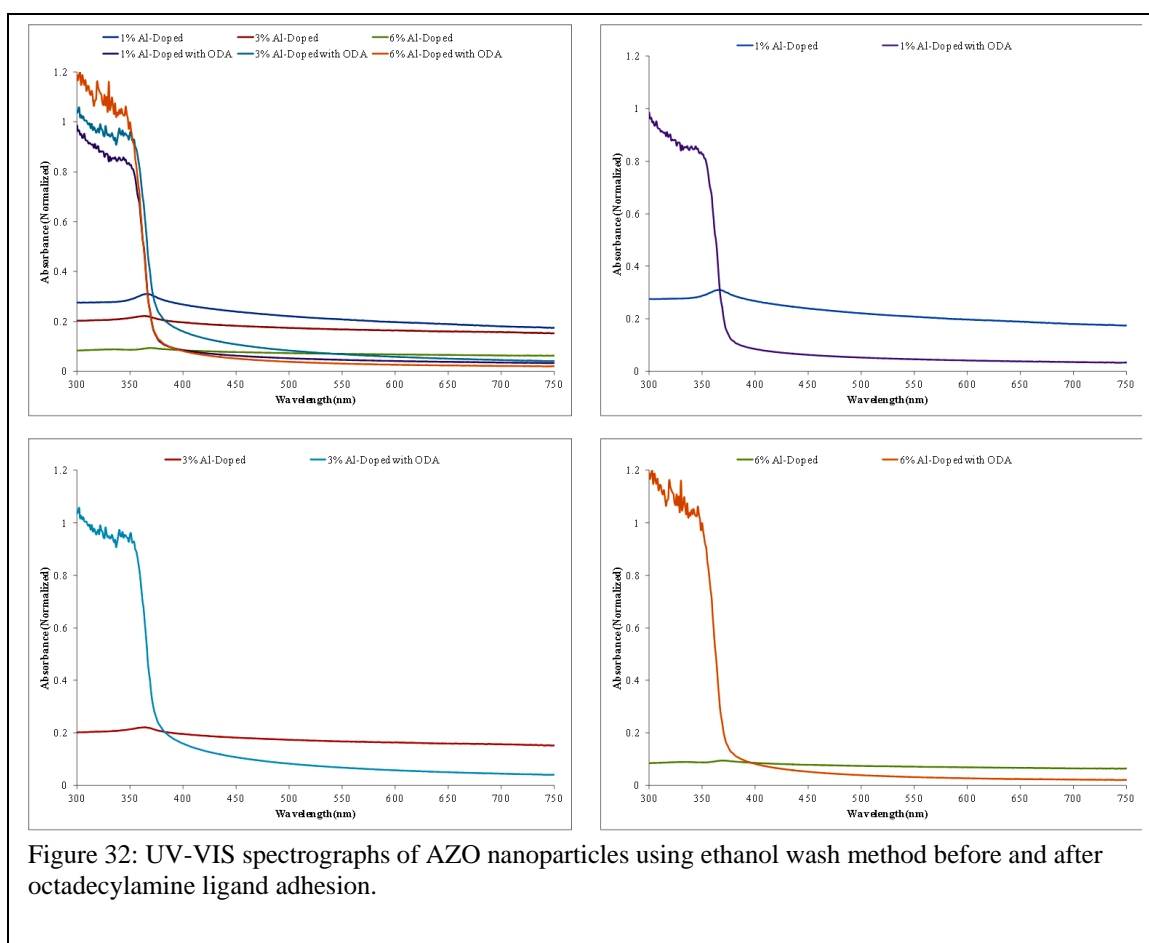
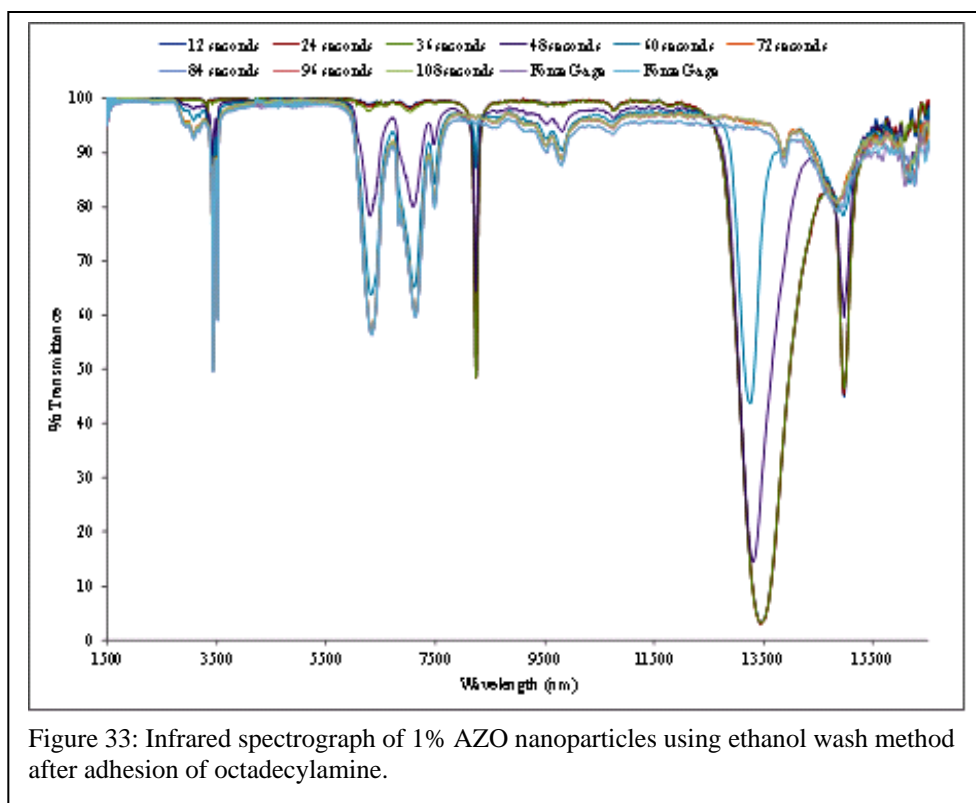
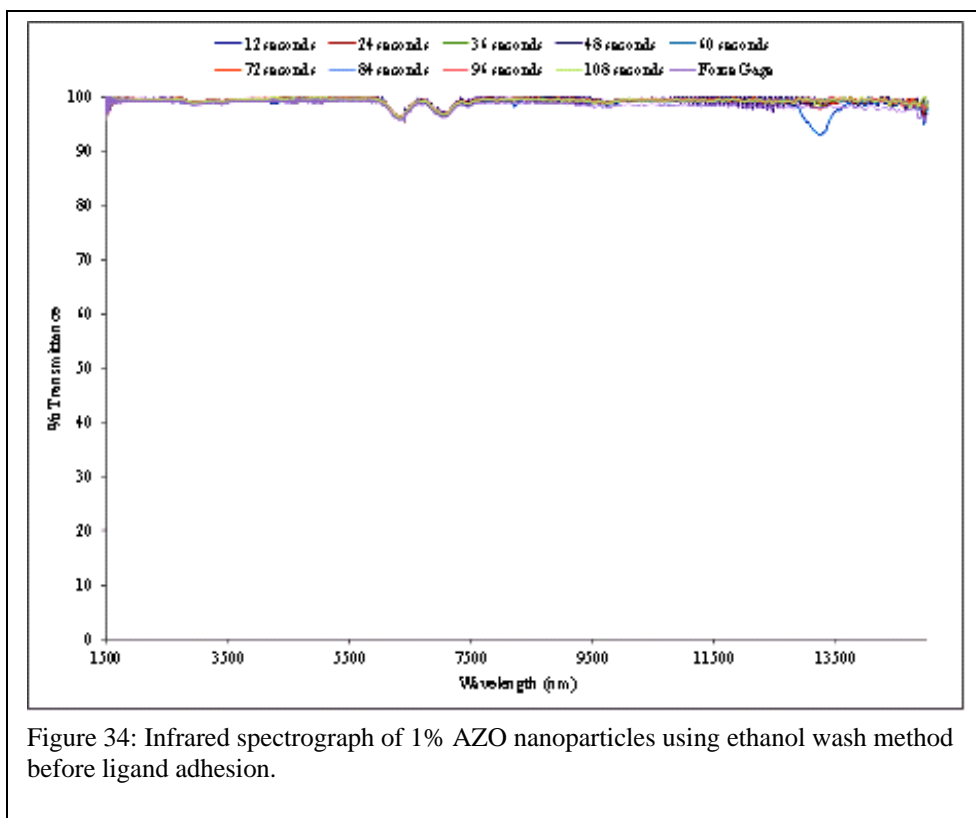


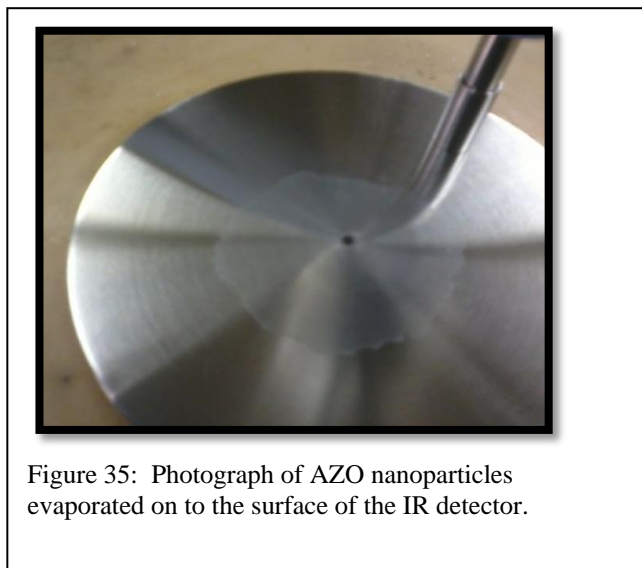
Table 9: UV-VIS spectrographs of AZO nanoparticles using the ethanol wash synthetic technique before and after ligand adhesion of octadecylamine.

AZO-Ethanol Wash Ligand Study	Maximum Peak	Normalized Maximum Peak	Wavelength (nm)	Difference in Wavelength (nm)	Shift in Wavelength	% Difference in Absorbance
1% Al-Doped	0.84	0.31	366			
1% Al-Doped with ODA	2.18	0.81	353	-13	Blue Shift	22%
3% Al-Doped	0.60	0.22	364			
3% Al-Doped with ODA	2.42	0.90	355	-9	Blue Shift	30%
6% Al-Doped	0.25	0.09	369			
6% Al-Doped with ODA	2.69	1.00	350	-19	Blue Shift	41%

Another way we can characterize the surface adhesion is from an infrared spectrograph. The AZO particles were suspended in chloroform and the IR spectra were taken every 12 seconds to monitor the transmittance as the particles become closer together. This was done to originally observe if the transmittance changes at these regions in the electromagnetic spectrum as the particle separation changes during the evaporation of the dispersive medium. In Figures 33 and 34 for 1% Al-doped ZnO the spectrograph shows that as the particles have incorporated octadecylamine as part of their matrix. The transmittance peaks for octadecylamine reduce once the dispersive medium evaporates. The peaks between 7500-9500 nm are the region to observe the ODA ligand.



An example of how well the AZO assembles with the organic ligand as the dispersive medium evaporates is shown in Figure 35.



We determine that the organic ligand enhances the quality of the AZO nanoparticles. The ligand helps to control the size of the nanoparticles which can reduce polydispersion broadening in UV-VIS spectra. The adhesion of the ligand allows a thin film of AZO nanoparticles to be layered onto any surface just drop casting a solution of the particles onto any surface. This gives a thought for future work to be done by spraying the particles onto a surface for controlled thickness and particle-particle uniformity.

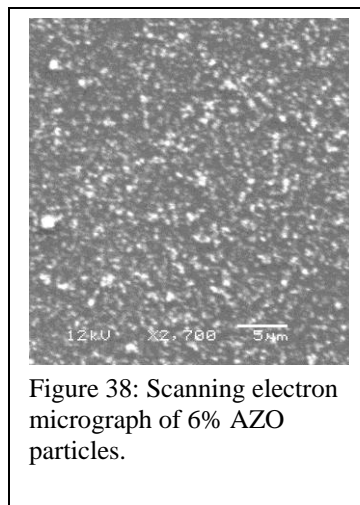
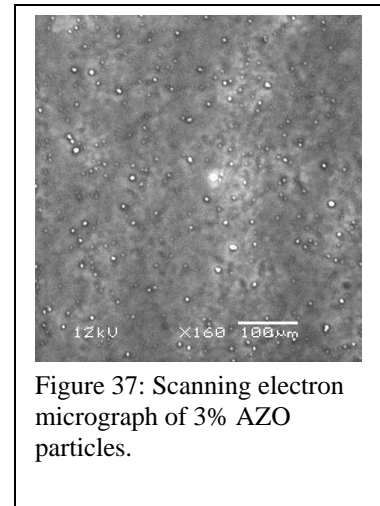
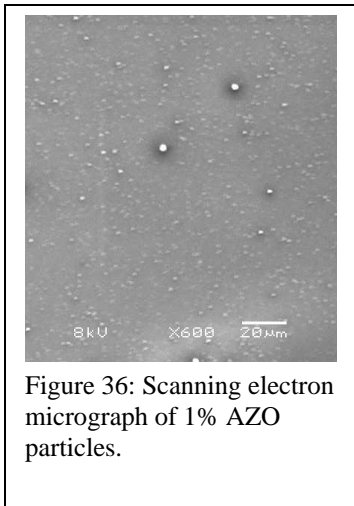
4.6 Measuring the index of AZO nanoparticles

The final stage of this work was to measure the surface boundary impedance or the index of the low loss metamaterial designed. We used ellipsometry to measure the index and the results were phenomenal and not expected to this extent.

In Figures 36, 37 and 38 we can observe the distribution of the particles.

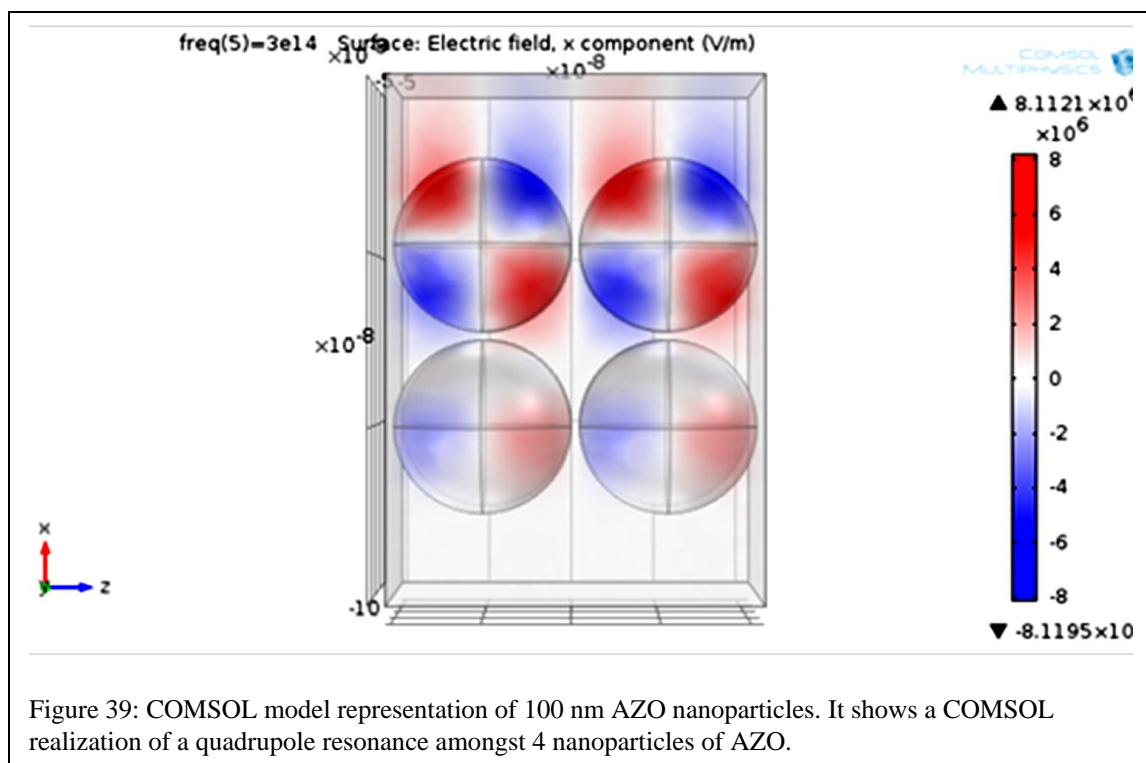
Elemental analysis was done on each sample and it was determined that 1% AZO obtained 0.60% Al, 3% AZO contained 0.56% Al, and 6% AZO contained 0.95% Al.

These samples were taken for a small area on the micrograph. The take home message is that aluminum is present in each of the samples which is a requirement for designing our low loss metamaterial.



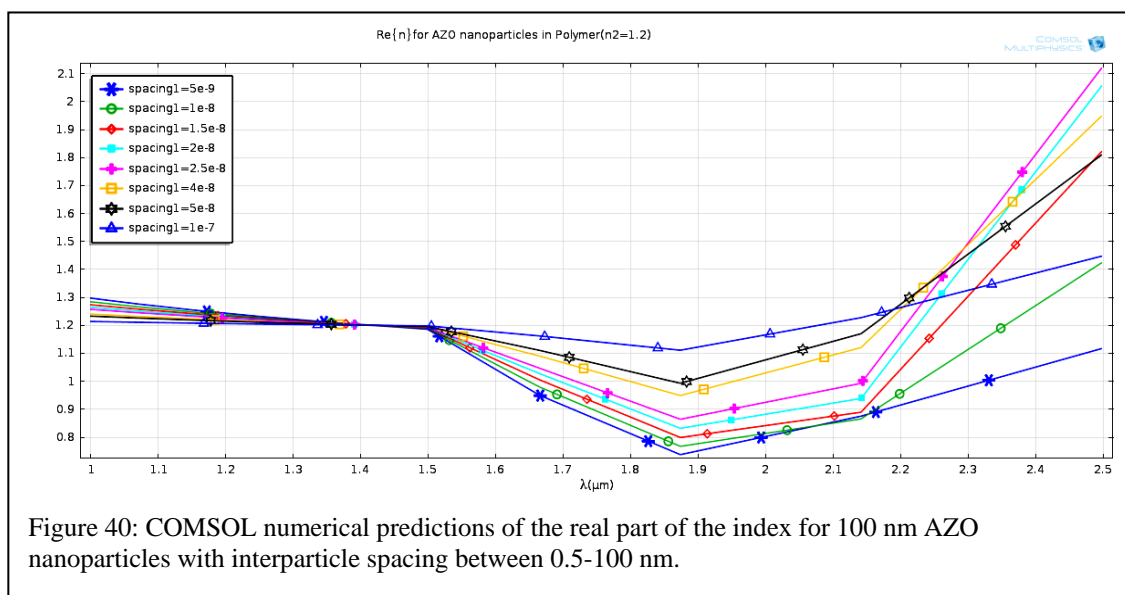
We measured the refractive index for all three samples of AZO nanoparticles and found that 1% AZO had an observed index of less than unity. The quadrupole resonance representation of the COMSOL numerical model is seen in Figure 39. As the applied electromagnetic field excites the AZO spheres the quadrupole resonance is a result of radiative coupling.⁹¹ We saw similar coupling effects in Chapter III for gold nanoparticles and AZO nanoparticles. However, this coupling of resonances is produced by localized surface plasmons. Our COMSOL simulations also predicted an index of less than unity shown in Figures 40 and 42. The simulations observe a drop in the index between 1.7 and 2.0 microns for 100 nm AZO nanoparticles surrounded by a polymer where its index is 1.2. The index of octadecylamine is 1.4 at 20°C.⁹²

The data in Figures 41 and 44 proves our hypothesis that a low loss metamaterial can be designed from AZO nanoparticles with not only controlled spacing but by the



couplings of two or four nanoparticles. This result is close to our numerical predictions. It also indicated that Professor Alexander Ramm is correct in that the recipe for designing a material of less than unity relies on increasing the scattering events to induce radiative coupling.

We ran numerical simulations for particles between 5-100 nm diameters. The COMSOL simulation of four particles 50 nm in radius we saw low index values at low optical frequencies (i.e. longer wavelengths). It appeared that the separation between these four particles still produced this coupling affect for lower index between 5-25 nm. However, in the data from the ellipsometer, there is a shift in the frequency at which the index of less than unity occurs. If we recall the radius of the 1% AZO with ODA ligand was 21 nm. The smaller particle has a plasmon resonance at a different frequency than that of our 50 nm radius simulated particles. Therefore the low index is at higher optical frequencies (i.e. shorter wavelengths). The strange behavior in regards to the sharp and dramatic swing of the imaginary part of the index (k) from the ellipsometry data is



unclear. It may be from internal reflection due to the substrate; however the substrate was a silicon wafer with a roughened backside. We note the dramatic difference in the ellipsometer data between the AZO nanoparticle-coated silicon wafer and the same wafer without particles, as shown in figure 43.

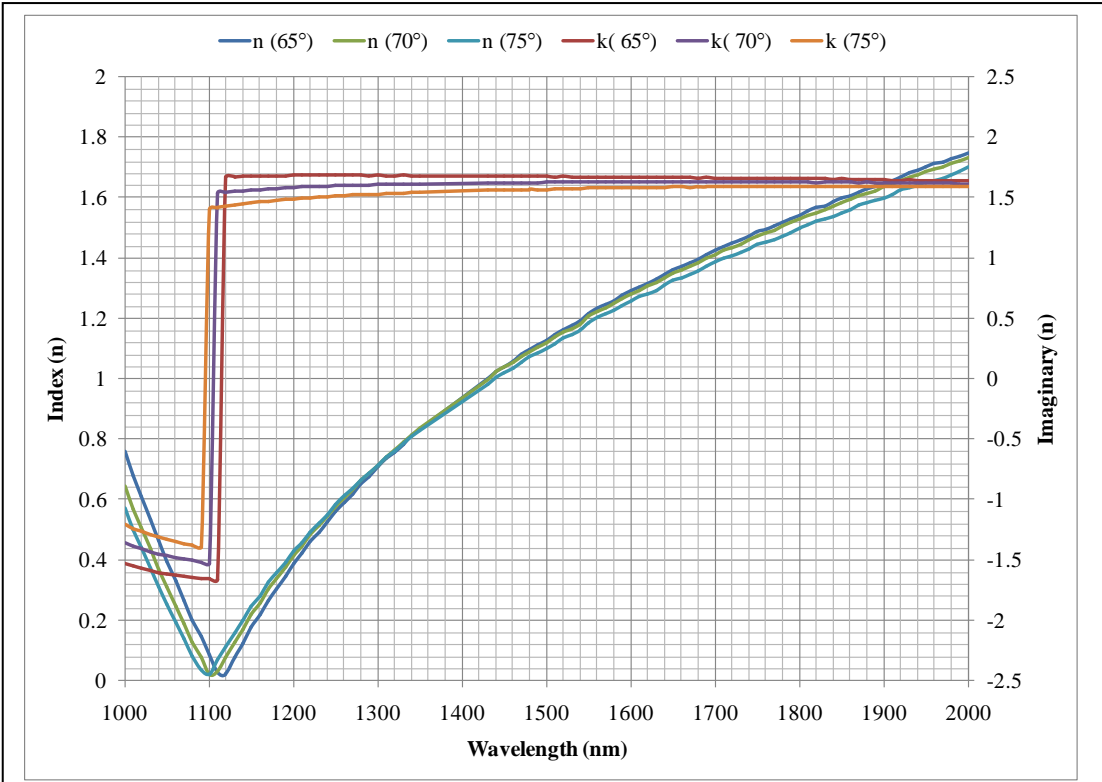


Figure 41: Index of 1% AZO thin film using UV-NIR Ellipsometer.

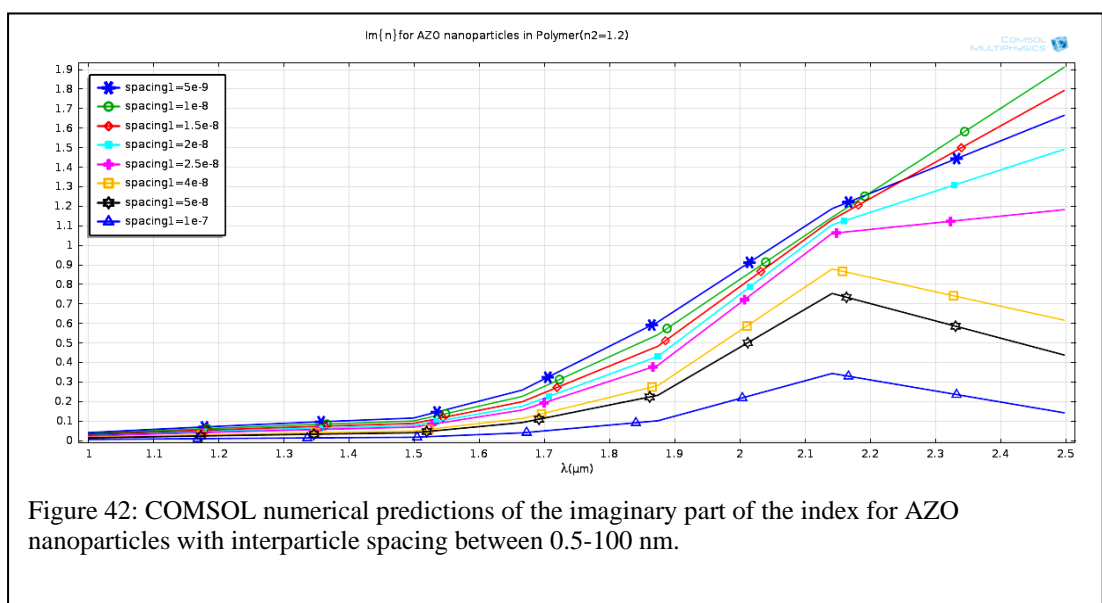


Figure 42: COMSOL numerical predictions of the imaginary part of the index for AZO nanoparticles with interparticle spacing between 0.5-100 nm.

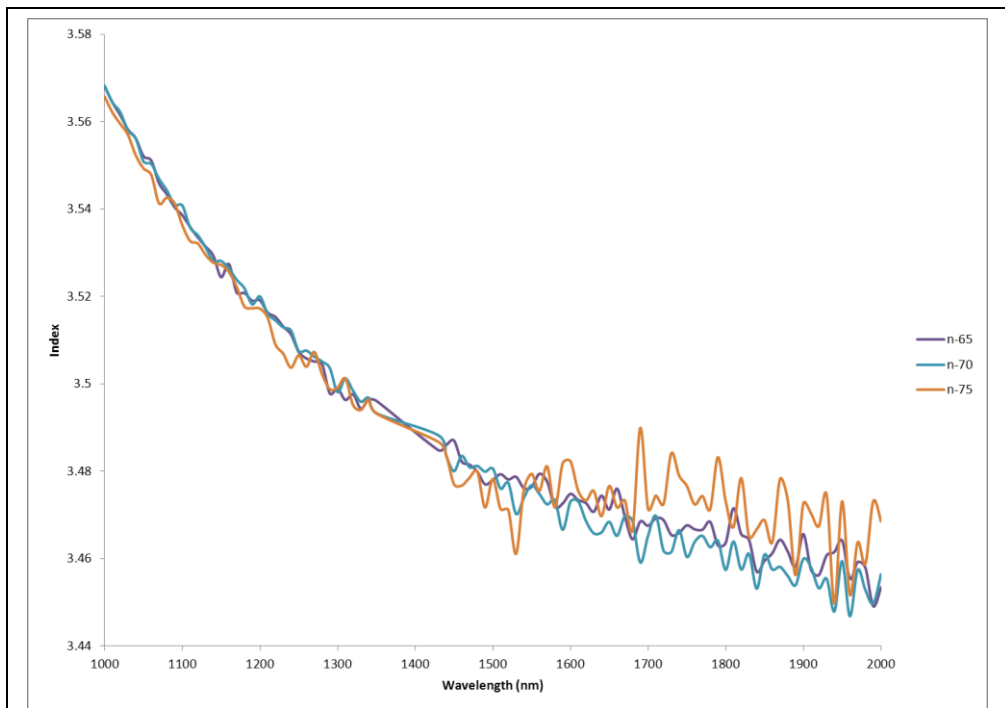


Figure 43: Index of refraction of silicon wafer using UV-NIR Ellipsometer.

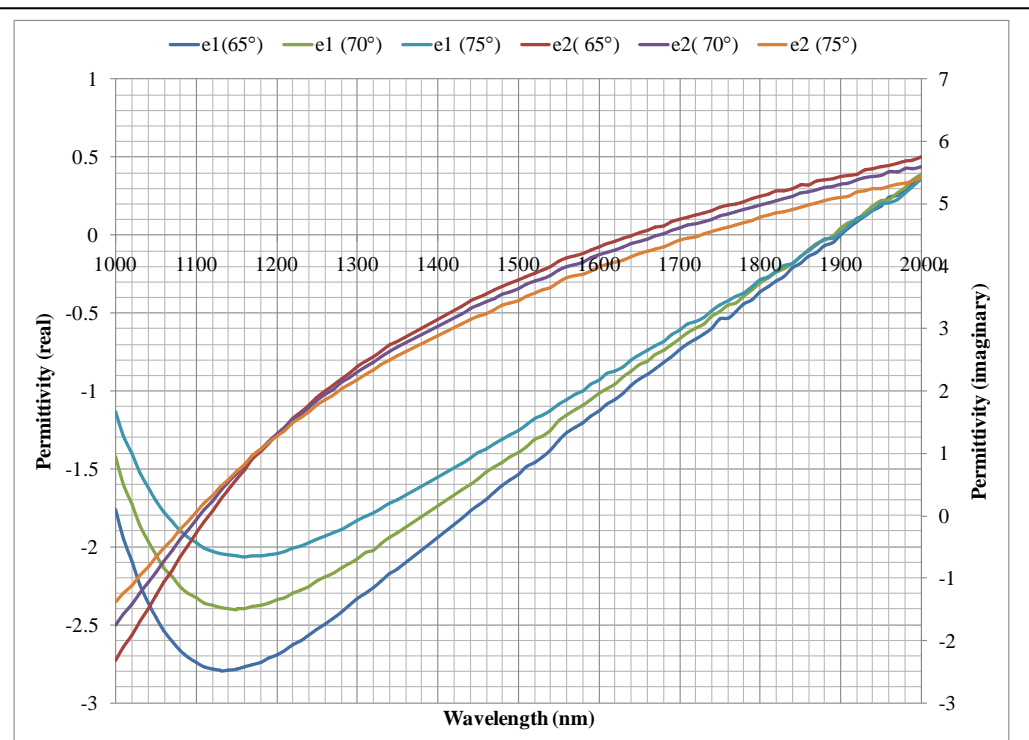


Figure 44: Permittivity of 1% AZO using UV-NIR Ellipsometer.

The permittivity shown in Figure 44 illustrates that the material has a negative permittivity around 2 at 1.1 microns wavelength, which interestingly is the value for maximum scattering. The values for the real part of the permittivity (ϵ_1) are negative which is reasonable for a transparent oxides. The values for the imaginary part of the permittivity (ϵ_2) are negative between 1000-1100 nm and the imaginary part of the index has small values. This is a bonus because what we set out to accomplish was to have the loss term be as small as possible, and for AZO nanoparticles this appears to be the case.

CHAPTER V: CONCLUSION

5.1 Research objectives revisited

1) Can a material with an index of less than unity be realized by increasing a composite material's scattering properties to drive down the index, and by altering particle-particle separation?

The answer to the question is yes, we have shown through numerical simulations and experimental data that this is possible. We discovered that driving down the index is also a matter of increasing the scattering dynamic of the particles and electromagnetic field coupling between the particles.

2) Is this material predicted using Dr. Ramm's theoretical model or by well-known mixing formula?

The answer to this question is somewhat and no. Even though, Dr. Ramm's theoretical model entails increasing the number of scatterers in some volume, we showed numerically that the requirement for driving the index to less than unity depends not only on strong scattering but also on coupling driven by the resonance of particles in close proximity, as well as the particle density. This was represented in our COMSOL simulations and experimental findings. We used a thin film of AZO nanoparticles and achieved a similar result in congruence with the COMSOL simulations.

3) Can High Frequency Structure Simulations (HFSS), COMSOL Physics, and Matlab provide supporting evidence for experimental findings?

The answer to this question is a definitive yes. The numerical predictions of the medium made from AZO nanoparticles were qualitatively similar to the experimental data. Some parameters are still unknown such as the quantity of aluminum in the materials that were made. Knowing the amount of aluminum can help refine more predictive numerical computations.

5.2 Insights and Interpretations

We made a low loss material fabricated from spherical nanoparticles using numerical predictive models. We explored different growth techniques for designing these nanoparticles. We discovered that rinsing the excess organometallic precursors with ethanol was the best way to control the size and morphology of the particles. It can also be stated that the control of size is strongly dependent on the rate at which lithium hydroxide is added to the zinc-aluminum ethanolic solution. If this process is not accurately controlled, the result is the growth of nanoparticles beyond the range of 150 nm. This was evident in our structural and optical characterization techniques.

Octadecylamine was the ligand that we used for our experimental work. ODA helped to separate particle sizes by only adhering to smaller particles. This is believed to be due to the concentration of ODA used in the synthesis. The ODA is roughly a nanometer in length and this distance from the surface may have aided the particles in scattering more efficiently because they were not touching due to the ligand as the protective barrier.

From our simulations we determined that a spherical particle with increased scattering was one required factor to have an index of less than unity. We also learned that we needed the loss term to be low so that the effective index would be less than unity. Also, we established that this result for the index is driven by field coupling effects due to particle proximity. Specifically, we identified that a quadrupole resonance occurs when the index is less than unity. It is our belief that both of these factors contribute to lead to an index of less than unity, i.e. we require both an increased scattering response and particle proximity.

The ellipsometry data showed that the index of AZO nanoparticles on a silicon substrate has an index of less than unity and that the loss term is relatively low. These data were similar to our COMSOL (quadrupole) simulations but at a slightly higher frequency due to the particle size difference. It is believed that the quadrupole resonance is responsible for giving a phase advance and hence light traveling through this material appears to have a phase velocity faster than the speed of light in vacuum. This means that transparent conducting oxide nanoparticles could contribute to the future of telecommunications, radar technologies, imaging, etc.

5.3 Future Work

In the future we should explore more ways to control the morphology of the nanoparticles. The SEM revealed many amorphous shapes. We could use a polyol synthetic technique using materials such as diethylene glycol (DEG) which is more viscous than ethanol to help aid in reaching more spherical nanoparticles.⁹³⁻⁹⁵ We note that uniformity of particle shape is important and are not saying that only spherical particles could be used to effect a low index material. Also if the sol-gel method is

continued, having the ability to control the reaction rate is necessary, meaning the drop-rate of the lithium hydroxide into the zinc-aluminum ethanolic solution. One could control this by using a syringe pump or wide valve separatory funnel.

In the future we can explore other types of ligands. We can try to interconnect the ligand by using a bidentate ligand as a more exact spacer. A large molecule such as a crown ethers, porphyrins, and even proteins can be candidates for spacing nanoparticles. This work would involve determining whether the material will adhere to the surface of a nanostructure effectively. Another suggestion is to use a ligand with a highly polar end group that is strong enough to overcome the electrostatic forces of AZO nanoparticles and thus space the particles by columbic forces.

The immediate next stage of this research would be quantifying the amount of aluminum incorporated, using Thermogravimetric Analysis (TGA). This is an excellent tool to determine how well each method of aluminum doping achieves the greatest amount of aluminum incorporated into the nanoparticles. To measure the conductivity of the nanoparticles on the film we could measure the resistivity using a four point probe. Conductivity was a part of our simulation and comparing the effects of the conductive nature of the particles on the index is something that should be done in the future. We saw from the HFSS numerical model that decreasing the conductivity of the nanoparticles drives the minimum index to higher values.

Also, it is important to determine what caused the emission spectra to diminish for the ethanol wash method; it appears to be correlated with increasing aluminum content. Two ways to characterize this phenomenon are to determine if aluminum oxide (Al_2O_3) is a factor in lower the emission is by Atomic Absorption Spectroscopy and Ionized

Coupled Plasma-Mass Spectroscopy. The two methods can detect trace amounts of metals. Therefore, during the synthesis of AZO nanoparticles taking samples of the solution at the initial stages and measuring the amount and type of metal can offer some clues to the decrease in the emission spectra.

Another area to explore is analyzing how spraying the particles onto a surface affects the resulting effective bulk index. The particles would be evenly dispersed and depending on the atomizer the thickness of the thin film could be readily controlled.

Finally, there is a need for more numerical predictions/simulations for these types of transparent conducting oxides. The next researcher should conduct experiments to analyze quadrupole and higher order resonances for nanoparticle distributions with radii from 5-50 nm. By doing this the behavior of the ellipsometry data could be better interpreted and justified for the optical frequencies of interest. Also, there needs to be a better understanding of these types of resonances as they relate to AZO nanoparticles for lowering the bulk index values, and to determine how a quadrupole or higher order resonance can cause a phase advance.

5.4 Summary

In summary the AZO nanoparticles as a constituent in a low loss metamaterial has great potential for the future. Even though this is just the beginning of investigating these transparent oxide materials for achieving a metamaterial with a refractive index of less than unity, it is a dramatic start. We have been able to show that by controlling the spacing of particles by ligand adhesion and clusters of particles become coupled and we can realize a material with an unusual refractive index, e.g. of less than one with low loss.

We began by investigating the theory proposed by Ramm that gives a target index for a distribution of subwavelength sized spherical particles. We established that we needed strong multiple scattering to drive the index down, which his theory predicts, but his model does not include coupling between closely spaced particles, which we also established contributes to a low index. We studied using low loss materials for the nanoparticles with a permittivity equal to -2 to achieve very strong resonant scattering, and found it to be lead to an index less than unity. With conducting particles we see the particles' scattering increasing when they are close, however the conductivity of each nanoparticle cannot be too high or this effect might be hampered according to the HFSS simulations because of associated losses.

We made a thin film of AZO nanoparticles that was less than one micron thick using octadecylamine as an interparticle separator, and were successful in assembling the particles uniformly onto a surface.

We also successfully synthesized AZO nanoparticles using a method that takes less than 24 hours for its conclusion. The particles were large with some of the methods, e.g. > 1 micron) used but using the ethanol wash synthetic method was the best choice for this body of work.

Finally, there are still numerous future directions to explore with this work. The applications in all of optics for low index films and media are vast. The next stages of this work would be to literally bottle the particles and spray or paint them onto a surface. This may not seem plausible for the moment but there is nothing fundamental to prevent it.

We hope that this dissertation and work can set future researchers on a path of discovery and innovation for fabricating and designing low loss and low index optical

metamaterials. This research has posed many new questions and some answers for those who pursue this. We hope that this work is continued and can one day benefit the world as a whole.

REFERENCES

1. Solymar, L., Shamonina, Ekaterina, *Waves in Metamaterials*. Oxford University Press Inc.; New York, 2009; p 385.
2. Soukoulis, C. M.; Wegener, M., Past achievements and future challenges in the development of three-dimensional photonic metamaterials. *Nature Photonics* 2011, 5 (9), 523-530.
3. Grzegorzczak, T. M.; Kong, J. A., Review of left-handed metamaterials: Evolution from theoretical and numerical studies to potential applications. *Journal of Electromagnetic Waves and Applications* 2006, 20 (14), 2053-2064.
4. Alivisatos, A. P., Birth of a nanoscience building block. *Acs Nano* 2008, 2 (8), 1514-1516.
5. Talapin, D. V.; Lee, J. S.; Kovalenko, M. V.; Shevchenko, E. V., Prospects of Colloidal Nanocrystals for Electronic and Optoelectronic Applications. *Chemical Reviews* 2010, 110 (1), 389-458.
6. Engheta, N., Circuits with light at nanoscales: Optical nanocircuits inspired by metamaterials. *Science* 2007, 317 (5845), 1698-1702.
7. Ramm, A. G., Electromagnetic wave scattering by many small bodies and creating materials with a desired refraction coefficient. *Progress In Electromagnetics Research M* 2010, 13, 203-215.
8. Zheludev, N. I., The Road Ahead for Metamaterials. *Science* 2010, 328 (5978), 582-583.
9. Liu, Y. M.; Zhang, X., Metamaterials: a new frontier of science and technology. *Chemical Society Reviews* 2011, 40 (5), 2494-2507.
10. Pendry, J. B., Negative refraction makes a perfect lens. *Physical Review Letters* 2000, 85 (18), 3966-3969.
11. Boltasseva, A.; Shalaev, V. M., Fabrication of optical negative-index metamaterials: Recent advances and outlook. *Metamaterials* 2008, 2 (1), 1-17.
12. K. Takada, h.-B. S., S. Kawata, Improved spatial resolution and surface roughness in photopolymerization-based laser nanowriting. *Appl.Phys.Lett* 2005, 86, 071122-71123.

13. Pendry, J. B.; Holden, A. J.; Robbins, D. J.; Stewart, W. J., Magnetism from conductors and enhanced nonlinear phenomena. *Ieee Transactions on Microwave Theory and Techniques* 1999, 47 (11), 2075-2084.
14. Linden, S. Split Ring Resonator compared with an LC circuit. <http://www.metaphotonics.de/metamaterials/atoms.html> (accessed December 1, 2011).
15. Wegener, M.; Linden, S., Shaping optical space with metamaterials. *Physics Today* 2010, 63 (10), 32-36.
16. Zhou, J.; Koschny, T.; Kafesaki, M.; Economou, E. N.; Pendry, J. B.; Soukoulis, C. M., Saturation of the Magnetic Response of Split-Ring Resonators at Optical Frequencies. *Physical Review Letters* 2005, 95 (22), 223902.
17. Klein, M. W.; Enkrich, C.; Wegener, M.; Soukoulis, C. M.; Linden, S., Single-slit split-ring resonators at optical frequencies: limits of size scaling. *Opt. Lett.* 2006, 31 (9), 1259-1261.
18. Sergei, T., On geometrical scaling of split-ring and double-bar resonators at optical frequencies. *Metamaterials* 2007, 1 (1), 40-43.
19. Zhang, S.; Fan, W. J.; Malloy, K. J.; Brueck, S. R. J.; Panoiu, N. C.; Osgood, R. M., Near-infrared double negative metamaterials. *Optics Express* 2005, 13 (13), 4922-4930.
20. Stoller, P.; Jacobsen, V.; Sandoghdar, V., Measurement of the complex dielectric constant of a single gold nanoparticle. *Los Alamos National Laboratory, Preprint Archive, Condensed Matter* 2006, 1-3, arXiv:cond-mat/0604174.
21. Johnson, P. B.; Christy, R. W., Optical-Constants of Noble-Metals. *Physical Review B* 1972, 6 (12), 4370-4379.
22. de, B. D. M.; Bremmer, R. H.; Kodach, V. M.; de, K. R.; van, M. J.; van, L. T. G.; Faber, D. J., Optical phantoms of varying geometry based on thin building blocks with controlled optical properties. *Journal of biomedical optics* 2010, 15 (2), 025001.
23. Nalwa.H.S, *Nanoclusters and Nanocrystals* American Scientific Publishers: 2003.
24. Frens, G., Controlled Nucleation for regulation of Particle-Size in monodisperse Gold Suspensions. *Nature-Physical Science* 1973, 241 (105), 20-22.

25. Kimling, J.; Maier, M.; Okenve, B.; Kotaidis, V.; Ballot, H.; Plech, A., Turkevich method for gold nanoparticle synthesis revisited. *Journal of Physical Chemistry B* 2006, *110* (32), 15700-15707.
26. Pei, L. H.; Mori, K.; Adachi, M., Formation process of two-dimensional networked gold nanowires by citrate reduction of AuCl₄⁻ and the shape stabilization. *Langmuir* 2004, *20* (18), 7837-7843.
27. Bhargava, S. K.; Booth, J. M.; Agrawal, S.; Coloe, P.; Kar, G., Gold nanoparticle formation during bromoaurate reduction by amino acids. *Langmuir* 2005, *21* (13), 5949-5956.
28. Brust, M.; Walker, M.; Bethell, D.; Schiffrin, D. J.; Whyman, R., Synthesis of Thiol-Derivatized Gold Nanoparticles in a 2-Phase Liquid-Liquid System. *Journal of the Chemical Society-Chemical Communications* 1994, (7), 801-802.
29. Garcia-Raya, D.; Madueno, R.; Blazquez, M.; Pineda, T., Electrochemistry of Molecule-like Au(25) Nanoclusters Protected by Hexanethiolate. *Journal of Physical Chemistry C* 2009, *113* (20), 8756-8761.
30. Jimenez, V. L.; Georganopoulou, D. G.; White, R. J.; Harper, A. S.; Mills, A. J.; Lee, D. I.; Murray, R. W., Hexanethiolate monolayer protected 38 gold atom cluster. *Langmuir* 2004, *20* (16), 6864-6870.
31. Zhang, J. L.; Du, J. M.; Han, B. X.; Liu, Z. M.; Jiang, T.; Zhang, Z. F., Sonochemical formation of single-crystalline gold nanobelts. *Angewandte Chemie-International Edition* 2006, *45* (7), 1116-1119.
32. Huang, S. X.; Ma, H. Y.; Zhang, X. K.; Yong, F. F.; Feng, X. L.; Pan, W.; Wang, X. N.; Wang, Y.; Chen, S. H., Electrochemical synthesis of gold nanocrystals and their 1D and 2D organization. *Journal of Physical Chemistry B* 2005, *109* (42), 19823-19830.
33. Yu, Y. Y.; Chang, S. S.; Lee, C. L.; Wang, C. R. C., Gold nanorods: Electrochemical synthesis and optical properties. *Journal of Physical Chemistry B* 1997, *101* (34), 6661-6664.
34. Jana, N. R.; Gearheart, L.; Murphy, C. J., Seeding growth for size control of 5-40 nm diameter gold nanoparticles. *Langmuir* 2001, *17* (22), 6782-6786.
35. Zhong, Z. Y.; Male, K. B.; Luong, J. H. T., More recent progress in the preparation of Au nanostructures, properties, and applications. *Analytical Letters* 2003, *36* (15), 3097-3118.

36. Henglein, A., Nanoclusters of semiconductors and metals: Colloidal nano-particles of semiconductors and metals: Electronic structure and processes. *Berichte der Bunsengesellschaft für physikalische Chemie* 1997, *101* (11), 1562-1572.
37. Mafune, F.; Kohno, J.; Takeda, Y.; Kondow, T.; Sawabe, H., Formation of gold nanoparticles by laser ablation in aqueous solution of surfactant. *Journal of Physical Chemistry B* 2001, *105* (22), 5114-5120.
38. Love, C. S.; Chechik, V.; Smith, D. K.; Wilson, K.; Ashworth, I.; Brennan, C., Synthesis of gold nanoparticles within a supramolecular gel-phase network. *Chemical Communications* 2005, (15), 1971-1973.
39. Fukuoka, A.; Araki, H.; Kimura, J.; Sakamoto, Y.; Higuchi, T.; Sugimoto, N.; Inagaki, S.; Ichikawa, M., Template synthesis of nanoparticle arrays of gold, platinum and palladium in mesoporous silica films and powders. *Journal of Materials Chemistry* 2004, *14* (4), 752-756.
40. Hirschwald, W. H., Zinc-oxide-An outstanding example of Binary Compound Semiconductor. *Accounts of Chemical Research* 1985, *18* (8), 228-234.
41. Wang, Z. L., Zinc oxide nanostructures: growth, properties and applications. *Journal of Physics-Condensed Matter* 2004, *16* (25), R829-R858.
42. Klingshirn, C., ZnO: Material, physics and applications. *Chemphyschem* 2007, *8* (6), 782-803.
43. Bunn, C. W., The lattice-dimensions of zinc oxide. *Proceedings of the Physical Society* 1935, *47* (5), 835.
44. Mang, A.; Reimann, K.; Rubenacke, S., Band-Gaps, Crystal-Field Splitting, Spin-Orbit-Coupling, and Exciton Binding-Energies in ZnO under Hydrostatic-Pressure. *Solid State Communications* 1995, *94* (4), 251-254.
45. Thomas, D. G., The Exciton Spectrum of Zinc Oxide. *Journal of Physics and Chemistry of Solids* 1960, *15* (1-2), 86-96.
46. Bagnall, D. M.; Chen, Y. F.; Zhu, Z.; Yao, T.; Koyama, S.; Shen, M. Y.; Goto, T., Optically pumped lasing of ZnO at room temperature. *Applied Physics Letters* 1997, *70* (17), 2230-2232.
47. Reynolds, D. C.; Look, D. C.; Jogai, B., Optically pumped ultraviolet lasing from ZnO. *Solid State Communications* 1996, *99* (12), 873-875.

48. Zhang, Y.; Wen, Y. H.; Zheng, J. C.; Zhu, Z. Z., Direct to indirect band gap transition in ultrathin ZnO nanowires under uniaxial compression. *Applied Physics Letters* 2009, 94 (11), 3.
49. Look, D. C.; Reynolds, D. C.; Sizelove, J. R.; Jones, R. L.; Litton, C. W.; Cantwell, G.; Harsch, W. C., Electrical properties of bulk ZnO. *Solid State Communications* 1998, 105 (6), 399-401.
50. Janotti, A.; Van de Walle, C. G., Fundamentals of zinc oxide as a semiconductor. *Reports on Progress in Physics* 2009, 72 (12).
51. Shionya, S., Yen, W., *Phosphor Handbook*. 2nd ed.; CRC Press: Boca Raton, FL, 1997.
52. Laudise, R. A.; Ballman, A. A., Hydrothermal Synthesis of Zinc Oxide and Zinc Sulfide. *Journal of Physical Chemistry* 1960, 64 (5), 688-691.
53. Suscavage, M.; Harris, M.; Bliss, D.; Yip, P.; Wang, S. Q.; Schwall, D.; Bouthillette, L.; Bailey, J.; Callahan, M.; Look, D. C.; Reynolds, D. C.; Jones, R. L.; Litton, C. W., High quality hydrothermal ZnO crystals. *Mrs Internet Journal of Nitride Semiconductor Research* 1999, 4, art. no.-G3.40.
54. Sekiguchi, T.; Miyashita, S.; Obara, K.; Shishido, T.; Sakagami, N., Hydrothermal growth of ZnO single crystals and their optical characterization. *Journal of Crystal Growth* 2000, 214, 72-76.
55. Ohshima, E.; Ogino, H.; Niikura, I.; Maeda, K.; Sato, M.; Ito, M.; Fukuda, T., Growth of the 2-in-size bulk ZnO single crystals by the hydrothermal method. *Journal of Crystal Growth* 2004, 260 (1-2), 166-170.
56. Haupt, M.; Ladenburger, A.; Sauer, R.; Thonke, K.; Glass, R.; Roos, W.; Spatz, J. P.; Rauscher, H.; Riethmuller, S.; Moller, M., Ultraviolet-emitting ZnO nanowhiskers prepared by a vapor transport process on prestructured surfaces with self-assembled polymers. *Journal of Applied Physics* 2003, 93 (10), 6252-6257.
57. Maeda, K.; Sato, M.; Niikura, I.; Fukuda, T., Growth of 2 inch ZnO bulk single crystal by the hydrothermal method. *Semiconductor Science and Technology* 2005, 20 (4), S49-S54.
58. Nause, J.; Nemeth, B., Pressurized melt growth of ZnO boules. *Semiconductor Science and Technology* 2005, 20 (4), S45-S48.

59. Lau, C. K.; Tiku, S. K.; Lakin, K. M., Growth of Epitaxial ZnO Thin-Films by Organometallic Chemical Vapor-Deposition. *Journal of the Electrochemical Society* 1980, 127 (8), 1843-1847.
60. Liu, Y.; Gorla, C. R.; Liang, S.; Emanetoglu, N.; Lu, Y.; Shen, H.; Wraback, M., Ultraviolet detectors based on epitaxial ZnO films grown by MOCVD. *Journal of Electronic Materials* 2000, 29 (1), 69-74.
61. Sallet, V.; Rommeluere, J. F.; Lusson, A.; Riviere, A.; Fusil, S.; Gorochov, O.; Triboulet, R., MOCVD growth of ZnO on sapphire using tert-butanol. *Physica Status Solidi B-Basic Research* 2002, 229 (2), 903-906.
62. Ive, T.; Ben-Yaacov, T.; Van de Walle, C. G.; Mishra, U. K.; DenBaars, S. P.; Speck, J. S., Step-flow growth of ZnO(0001) on GaN(0001) by metalorganic chemical vapor epitaxy. *Journal of Crystal Growth* 2008, 310 (15), 3407-3412.
63. Fons, P.; Tampo, H.; Kolobov, A. V.; Ohkubo, M.; Niki, S.; Tominaga, J.; Carboni, R.; Boscherini, F.; Friedrich, S., Direct observation of nitrogen location in molecular beam epitaxy grown nitrogen-doped ZnO. *Physical Review Letters* 2006, 96 (4).
64. Johnson, M. A. L.; Fujita, S.; Rowland, W. H.; Hughes, W. C.; Cook, J. W.; Schetzina, J. F., MBE growth and properties of ZnO on sapphire and SiC substrates. *Journal of Electronic Materials* 1996, 25 (5), 855-862.
65. Heinze, S.; Krtschil, A.; Blaesing, J.; Hempel, T.; Veit, P.; Dadgar, A.; Christen, J.; Krost, A., Homoepitaxial growth of ZnO by metalorganic vapor phase epitaxy in two-dimensional growth mode. *Journal of Crystal Growth* 2007, 308 (1), 170-175.
66. Ardakani, H. K., Electrical conductivity of in situ "hydrogen-reduced" and structural properties of zinc oxide thin films deposited in different ambients by pulsed excimer laser ablation. *Thin Solid Films* 1996, 287 (1-2), 280-283.
67. Quaranta, F.; Valentini, A.; Rizzi, F. R.; Casamassima, G., DUAL-ION-BEAM SPUTTER-DEPOSITION OF ZNO FILMS. *Journal of Applied Physics* 1993, 74 (1), 244-248.
68. Spanhel, L.; Anderson, M. A., Semiconductor Clusters in the Sol-Gel Process-Quantized Aggregation, Gelation, and Crystal-Growth in Concentrated ZnO Colloids. *Journal of the American Chemical Society* 1991, 113 (8), 2826-2833.
69. Veselago, V. G., Electrodynamics of Substances with Simultaneously Negative Values of Sigma and Mu. *Soviet Physics Uspekhi-Ussr* 1968, 10 (4), 509-&.

70. Sivukhin, D. V., The energy of electromagnetic waves in dispersive media. *Opt. Spectrosc* 1957, 3, 308-312.
71. Smith, D. R.; Padilla, W. J.; Vier, D. C.; Nemat-Nasser, S. C.; Schultz, S., Composite medium with simultaneously negative permeability and permittivity. *Physical Review Letters* 2000, 84 (18), 4184-4187.
72. Born, M., Wolf, E., *Principles of Optics*. 6th ed.; New York: Pergamon: 1980.
73. Ramakrishna, S. A., Physics of negative refractive index materials. *Reports on Progress in Physics* 2005, 68 (2), 449-521.
74. Kubo, S.; Diaz, A.; Tang, Y.; Mayer, T. S.; Khoo, I. C.; Mallouk, T. E., Tunability of the Refractive Index of Gold Nanoparticle Dispersions. *Nano Letters* 2007, 7 (11), 3418-3423.
75. Pei, Y.; Yao, F.; Ni, P.; Sun, X., Refractive index of silver nanoparticles dispersed in polyvinyl pyrrolidone nanocomposite. *Journal of Modern Optics* 2010, 57 (10), 872-875.
76. Yannopoulos, V., Subwavelength imaging of light by arrays of metal-coated semiconductor nanoparticles: a theoretical study. *Journal of Physics: Condensed Matter* 2008, 20 (25), 255201/1-255201/8.
77. Ramm, A. G., A Method for Creating materials with a Desired Refraction Coefficient. *International Journal of Modern Physics B* 2010, 24 (27), 5261-5268.
78. Link, S.; El-Sayed, M. A., Shape and size dependence of radiative, non-radiative and photothermal properties of gold nanocrystals. *International Reviews in Physical Chemistry* 2000, 19 (3), 409-453.
79. Creighton, J. A.; Eadon, D. G., Ultraviolet-visible absorption spectra of the colloidal metallic elements. *Journal of the Chemical Society, Faraday Transactions* 1991, 87 (24), 3881-3891.
80. Ari, S., Mixing Rules. In *Theory and Phenomena of Metamaterials*, CRC Press: 2009.
81. Dyck, N. C.; Denomme, R. C.; Nieva, P. M., Effective Medium Properties of Arbitrary Nanoparticle Shapes in a Localized Surface Plasmon Resonance Sensing Layer. *Journal of Physical Chemistry C* 2011, 115 (31), 15225-15233.

82. Stoller, P.; Jacobsen, V.; Sandoghdar, V., Measurement of the complex dielectric constant of a single gold nanoparticle. *Optics Letters* 2006, *31* (16), 2474-2476.
83. De Sousa, F. F., Mreira, Sanclayton G. C., dos Santos da Silva, Shirsley J.; Del Nero, J., and Alcantara, Petrus, Dielectric Properties of Oleic Acid in Liquid Phase. *Journal of Bioscience* 2010, *3*, 1-4.
84. Fontana, J.; Naciri, J.; Rendell, R.; Ratna, B. R., Macroscopic Self-Assembly and Optical Characterization of Nanoparticle–Ligand Metamaterials. *Advanced Optical Materials* 2013, *1* (1), 100-106.
85. West, P. R.; Ishii, S.; Naik, G. V.; Emani, N. K.; ShalaeV, V. M.; Boltasseva, A., Searching for better plasmonic materials. *Laser & Photonics Reviews* 2010, *4* (6), 795-808.
86. Meulenkamp, E. A., Synthesis and growth of ZnO nanoparticles. *Journal of Physical Chemistry B* 1998, *102* (29), 5566-5572.
87. Minami, T.; Nanto, H.; Takata, S., Highly Conductive and Transparent Aluminum Doped Zinc-Oxide Thin-Films Prepared by RF Magnetron Sputtering. *Japanese Journal of Applied Physics Part 2-Letters* 1984, *23* (5), L280-L282.
88. Hu, J. H.; Gordon, R. G., Textured Aluminum-Doped Zinc-Oxide Thin-Films from Atmospheric-Pressure Chemical-Vapor Deposition. *Journal of Applied Physics* 1992, *71* (2), 880-890.
89. Nakahara, K.; Tanabe, T.; Takasu, H.; Fons, P.; Iwata, K.; Yamada, A.; Matsubara, K.; Hunger, R.; Niki, S., Growth of undoped ZnO films with improved electrical properties by radical source molecular beam epitaxy. *Japanese Journal of Applied Physics Part 1-Regular Papers Short Notes & Review Papers* 2001, *40* (1), 250-254.
90. Brevnov, D. A.; Bungay, C., Diameter-Dependent Optical Constants of Gold Mesoparticles Electrodeposited on Aluminum Films Containing Copper. *Journal of Physical Chemistry B* 2005, *109* (30), 14529-14535.
91. Luk'yanchuk, B.; Zheludev, N. I.; Maier, S. A.; Halas, N. J.; Nordlander, P.; Giessen, H.; Chong, C. T., The Fano resonance in plasmonic nanostructures and metamaterials. *Nature Materials* 2010, *9* (9), 707-715.
92. CRC Handbook of Chemistry and Physics. 92nd Edition. *Anticancer research* 2012, *32* (5), 2220.

93. Li, C. G.; Zhao, Y.; Wang, L.; Li, G. H.; Shi, Z.; Feng, S. H., Polyol-Mediated Synthesis of Highly Water-Soluble ZnO Colloidal Nanocrystal Clusters. *European Journal of Inorganic Chemistry* 2010, (2), 217-220.
94. Chieng, B. W.; Loo, Y. Y., Synthesis of ZnO nanoparticles by modified polyol method. *Materials Letters* 2012, 73, 78-82.
95. Zheng, J.; Song, X. Z.; Liu, X. J.; Chen, W.; Li, Y.; Guo, J., Synthesis of hexagonal CoFe₂O₄/ZnO nanoparticles and their electromagnetic properties. *Materials Letters* 2012, 73, 143-146.

APPENDIX A: MATHEMATICAL CHARACTERS

Table 10: Mathematical Characters

n_0	Index of particle	ζ_m	Boundary Impedance
n	Index of environment	$\mathcal{N}(\Delta_p)$	Number of small inhomogeneities in an arbitrary open subset
a	Radius of particle	κ	Arbitrary number chosen
$p(x)$	Function determining the boundary impedance	$h(x)$	Function determining the boundary impedance
x_m	Points in the bound domain	y_p	Points in the bound domain
k	Wavenumber ($2\pi/\lambda$)	S	Area of the particle($4\pi a^2$)`
ε	Permittivity	μ	Permeability
ω	Frequency	γ	Damping Constant